

UTILIZING 3D PRINTING TECHNOLOGY IN WELL STIMULATION  
RESEARCH

A Thesis

by

GABRIEL ANTHONY TATMAN

Submitted to the Graduate and Professional School of  
Texas A&M University  
In partial fulfillment of the requirements for the degree of

MASTER OF SCIENCE

Chair of Committee	Ding Zhu
Co-Chair of Committee	Dan Hill
Committee Member	Victor Ugaz
Head of Department	Jeff Spath

May 2023

Major Subject: Petroleum Engineering

Copyright 2023 Tatman, Gabriel Anthony

## ABSTRACT

Multi-stage hydraulic fracturing has become common practice for economically enhancing production from unconventional oil and gas reservoirs in recent years. The process of hydraulic fracturing is continuously refined as we discover new techniques through field studies and laboratory investigations. However, in modern well stimulation research, it is often difficult or impossible to obtain core samples with consistent properties for experimental studies. In these cases, isolating & evaluating stimulation design parameters with differing samples can be problematic, as large variations in rock properties can lead to inconsistent or incorrect conclusions. Therefore, the ability to reliably procure core samples with the identical characteristics would serve to benefit the confidence in the results of laboratory investigations.

The aim of this work is to design a framework for utilizing 3D printing technology to consistently generate detailed artificial samples suitable for use in experimental laboratory research. Many readily available modern 3D printers can produce samples with up to 20-75 micrometers of accuracy. Stereolithographic (SLA) resin 3D printers accomplish this by using an ultraviolet light source to selectively illuminate and cure a photopolymer onto a travelling build platform, building a physical model in a layer-by-layer fashion. Recent developments in this technology also allow SLA 3D printers to generate large-volume samples without sacrificing speed and resolution.

For this study, two areas of well stimulation research were chosen to demonstrate the successful implementation of the presented workflow. In the first part of this work, we created a realistic, rough-walled fracture system with 3D printed surfaces that mimic those of actual fractured rock for use in proppant transport experiments. While the rough topography of fracture walls likely influences the proppant transport process in the reservoir, nearly all historical

laboratory flow studies of proppant transport have used parallel smooth surfaces to represent these fracture walls. The transparent, rough-walled fracture system created in this study allowed for the direct observation of proppant behavior as slurries were pumped. With transparent 3D printed samples that more accurately represent the surfaces of actual rock, we can elevate our understanding of the behavior of proppants, fluids, and additives in hydraulic fractures.

In the second focus of this study, casts of 3D printed samples with simulated rough fracture surfaces were used to create artificial cement replicas suitable for conductivity experiments. Core samples, even when originating from the same source, still can possess a large variability in surface topography due to the inherent irregular nature of fractures. To address this, 3D printed conductivity samples were used as a mold for producing cement samples to serve as an alternative for core. In this investigation, we found that these cement replicas were able to retain the desired surface geometry and resolution while maintaining the required compressive strength to withstand the closure stresses required for conductivity testing.

This work presents the detailed workflow for generating 3D printed samples and demonstrates the successful implementation of this workflow in the types of experimental studies mentioned above, aiming to serve as the foundation for the continued use throughout future investigations.

## DEDICATION

*This work is dedicated to my family:*

*To my parents, without whom I would not be the person I am today,*

*&*

*To my wife, Kate, for making our time at Texas A&M so memorable.*

## ACKNOWLEDGEMENTS

I would like to thank Dr. Ding Zhu and Dr. Daniel Hill for gifting me the opportunity to pursue a graduate degree in an area of research near and dear to my heart, especially at a time where I was unsure where my career would begin to take me. In sharing their perspective with me, I learned how to approach problems with an inquisitive mindset. Without their guidance and extensive knowledge, none of this work would have been possible.

Thanks to Dr. Jennifer Miskimins and Ph.D. Candidate Ashtiwi Bahri from the Colorado School of Mines for playing a large role in bringing this project to life. I learned much from our extensive discussions throughout the course of this work.

I thank Dr. Victor Ugaz of the Artie McFerrin Department of Chemical Engineering at Texas A&M University for his part in serving on the committee for this thesis.

Additionally, I would like to sincerely thank John Maldonado from the Harold Vance Department of Petroleum Engineering for all the help in the lab over the years. I could always rely on John for an answer when I was unsure of where else to search.

Lastly, I would like to thank those in my research group who supported me throughout my time in the department, with special thanks to Tohoko Tajima and Carrie Sistrunk for their contributions to this project. I know you will go on to continue to accomplish great things.

## **CONTRIBUTORS AND FUNDING SOURCES**

### **Contributors**

This work was part of a joint research project between Texas A&M University, the Colorado School of Mines, and sponsors of the 3D Printing Research for Well Stimulation Program. The thesis committee consists of Dr. Ding Zhu and Dr. Daniel Hill of the Harold Vance Department of Petroleum Engineering and Dr. Victor Ugaz of the Artie McFerrin Department of Chemical Engineering at Texas A&M University.

The code utilized for generating simulated fracture surfaces in this research was modified by Tohoko Tajima and myself from the Geostatistical Software Library (GSLIB) and the Geostats Py python library by Dr. Michael Pyrcz of the University of Texas at Austin.

The proppant transport experimental apparatus was assembled with the assistance of Ashtiwi Bahri from the Colorado School of Mines.

Lastly, the conductivity investigation of the cement samples was performed with help from M.S. candidates Carrie Sistrunk & Travis Brashear.

### **Funding Sources**

Graduate study was supported by a fellowship from Texas A&M University and a Research Assistant position in the Harold Vance Department of Petroleum Engineering. This work was also made possible through the generous funding provided by the sponsors of the Joint Investigative Project for 3D Printing Well Stimulation Research.

# TABLE OF CONTENTS

	Page
ABSTRACT.....	ii
DEDICATION.....	ii
ACKNOWLEDGEMENTS.....	iii
CONTRIBUTORS AND FUNDING SOURCES.....	iv
TABLE OF CONTENTS.....	v
LIST OF FIGURES.....	vii
1. INTRODUCTION.....	1
1.1 Background.....	1
1.2 Literature Review.....	2
1.2.1 Hydraulic Fracturing in Shales.....	2
1.2.2 Laboratory Measurement of Fracture Conductivity.....	3
1.2.3 Transport of Proppant in Hydraulic Fractures.....	7
1.2.4 Acid Fracture Conductivity.....	10
1.2.5 Types of 3D Printing & Prior Uses in Well Stimulation Research.....	11
1.3 Problem Description, Objectives and Significance.....	19
1.4 Dissertation Outline.....	20
2. EXPERIMENTAL DESIGN AND PROCEDURE.....	21
2.1 Introduction.....	21
2.2 Workflow for Generating 3D Models.....	21
2.2.1 Capturing Fracture Surface Roughness.....	22
2.2.2 Simulating Artificial Fracture Surfaces.....	24
2.2.3 Creating a Digital Fracture Model.....	26
2.3 3D Printing Workflow.....	27
2.3.1 Description of Printer Apparatus.....	28
2.3.2 Preparing a Digital Model for Printing.....	29
2.3.3 Printing & Post-processing Workflow.....	33
2.3.4 Sample Validation with Profilometer.....	35
2.4 Fracture Conductivity Sample Design.....	36
2.4.1 Creating a Digital Conductivity Model.....	37
2.4.2 Generating Conductivity Samples from 3D Prints.....	38
2.5 Proppant Transport Apparatus Design.....	39
2.6 Key Design Challenges & Considerations.....	41
3. RESULTS & DISCUSSION.....	43

3.1 Introduction.....	43
3.2 Proppant Transport Apparatus .....	43
3.3 Assembling the Transport Apparatus & Early Experimental Results .....	44
3.4 Conductivity Samples .....	46
4. CONCLUSIONS & RECOMMENDATIONS.....	51
4.1 Conclusions .....	51
4.2 Limitations, Recommendations, and Future Work .....	52
REFERENCES .....	53
APPENDIX A: 3D PRINTING NOMENCLATURE .....	58



## LIST OF FIGURES

	Page
Figure 1.1: Schematic of the experimental setup for conductivity measurement.....	4
Figure 1.2: Eagle Ford Shale Fracture Conductivity Samples.....	5
Figure 1.3: Fracture conductivity vs. fracture surface roughness for Nitrogen at 1,000 psi closure stress (Guerra, Zhu, & Hill, 2017).....	6
Figure 1.4: Fracture conductivity vs. fracture surface maximum height difference, dry nitrogen flow at 4,000 psi closure stress (Guerra, Zhu, & Hill, 2017). ....	7
Figure 1.5: Settling of sand injected in a fracture slot (Kern et. al , 1959).....	8
Figure 1.6: Experimental Proppant Transport Apparatus for Complex Slot Systems (Bahri & Miskimins, 2021).....	10
Figure 1.7: Speed vs. Accuracy for common 3D printing techniques (Anderson, 2016 .....	12
Figure 1.8 : Schematic of a Typical FDM 3D Printer (Olivera et. al, 2016) .....	12
Figure 1.9: Example of fused deposition modeling 3D printing process. ....	14
Figure 1.10: Digital elevation model of the natural discontinuity surfaces (Isleyen & Duzgun, 2018).....	14
Figure 1.11: Discontinuity replication procedure (Isleyen & Duzgun, 2018). ....	15
Figure 1.12: Layering of an early FDM Sample (Obi, 2021) .....	16
Figure 1.13: Schematic of a standard LCD resin 3D printer (Luongo, et al., 2019) .....	17
Figure 1.14: 3D printed large-scaled pore network (Anderson, 2016).....	18
Figure 2.1: Workflow for Producing 3D Printed Samples .....	21
Figure 2.2: Impact of Correlation Length & Std. Deviation on Surface Roughness .....	23
Figure 2.3: Simulated 6 X 6 in. surface with $\mu = 0.3$ in, $\sigma = 0.05$ in, $\lambda_{Dx} = \lambda_{Dy} = 0.5$ .....	24
Figure 2.4: Simulated 6 X 6 in. surface with $\mu = 0.3$ in, $\sigma = 0.05$ in, $\lambda_{Dx} = 0.5$ , $\lambda_{Dy} = 0.05$ .....	25
Figure 2.5: Simulated 6 X 6 in. surface with $\mu = 0.3$ in, $\sigma = 0.05$ in, $\lambda_{Dx} = 0.05$ , $\lambda_{Dy} = 0.05$ .....	25

Figure 2.6: 0.5 Simulated 6 X 6 in. surface with $\mu = 0.3$ in, $\sigma = 0.1$ in, $\lambda_{Dx} = 0.5$ , $\lambda_{Dy} = 0.05$ .....	26
Figure 2.7: A digital model of a fracture surface (Left) and a magnified view of the triangulated surface (Right) .....	27
Figure 2.8: Description of Printer Apparatus.....	28
Figure 2.9: Standard Resolution Settings for the Phrozen Transform 3D Printer .....	30
Figure 2.10: Optimal Settings for Transparent Resin on the Phrozen Transform Printer.....	31
Figure 2.11: Preview Generated from Slicing Software.....	32
Figure 2.12: 3D Printed Samples Curing under UV Light .....	34
Figure 2.13: Overview of Profilometer Set Up.....	35
Figure 2.14: Fracture Conductivity Cell.....	36
Figure 2.15: Generating Digital Model for Fracture Conductivity Cell Sample .....	38
Figure 2.16: Schematic of Proppant Transport Apparatus.....	39
Figure 2.17 : A single fracture panel being post-processed in isopropyl alcohol.....	40
Figure 2.18 : Two fracture panels. ....	40
Figure 3.1 : Matching Rough Fracture Surfaces.....	43
Figure 3.2: Side View of Single 1ft X 1 ft Transparent Fracture Tile .....	44
Figure 3.3 : Final Proppant Transport Apparatus .....	45
Figure 3.4 : Duning shown from Proppant Transport Experiment .....	45
Figure 3.5 : Digital Model (Left) and 3D Printed Sample (Right) .....	47
Figure 3.6 : Comparison of 3D Printed Profilometer Distribution and Modeled Distribution.....	48
Figure 3.7 : Cement replicas cast from mold of 3D printed conductivity samples .....	49
Figure 3.8 : Profilometer scans of 3D printed sample and cement replicates.....	49

# 1. INTRODUCTION

## 1.1 Background

In modern well stimulation research, it is often difficult or impossible to obtain core samples with consistent properties. In these instances, isolating & evaluating stimulation design parameters can be difficult, as large variations in rock properties can lead to incorrect or inconsistent conclusions. Therefore, the ability to reliably procure identical core samples for testing would serve to greatly benefit the confidence in any results that are influenced by multiple variables.

3D printing can be utilized to address this problem. Recent advancements in 3D printing technology allow for the manufacturing of precise samples at low costs. While this technology has existed for decades, the ability to produce large samples on the order of several feet in length in a timely manner is one advancement that has only occurred in recent years. Modern 3D printers can reach accuracies of 25-75 micrometers, which is more than adequate for use in a wide range of experimental core sample studies. Additionally, 3D printed materials have made significant progress over the past decade, such as the development of transparent printing resins and high-strength resins.

This work explores the advantages of leveraging 3D printing technology to generate consistent samples for studies, outlines a workflow for utilizing the 3D printing process in stimulation research, and demonstrates the successful application of this workflow for use in a proppant transport apparatus and in fracture conductivity sample generation.

## **1.2 Literature Review**

In this literature review, an introduction to hydraulic fracturing discussed in order to discuss the importance of well stimulation as well as what parameters are used to evaluate the effectiveness of a stimulation job.

Next, we review the literature for a few historical approaches for investigating these parameters in the laboratory. More specifically, the laboratory studies of proppant transport and fracture conductivity are discussed to highlight the importance of surface roughness in each of these processes, as surface roughness is something that can easily be controlled in 3D printed samples.

Finally, an introduction to 3D printing processes and a review of previous studies aimed at leveraging 3D printing in well stimulation are discussed to present the benefits and shortcomings of the technology in previous literature.

### **1.2.1 Hydraulic Fracturing in Shales**

Shale is a fine-grained, clastic sedimentary rock composed of mud that is a mixture of flakes of clay minerals and tiny fragments of other minerals, especially quartz and calcite (Blat, Tracy, & Owens, 2006). Shale rocks are highly laminated and natural fractures are commonly present throughout. The extremely low permeability of shale reservoirs, often on the order of nano-milli Darcy's, makes production from these formations difficult without adequate stimulation to boost production.

Hydraulic fracturing is a stimulation method to enhance well productivity in these tight reservoirs by injecting viscous, proppant-loaded fluids at a pressure that exceeds the

formation fracturing pressure. After treatment, the injected fluids leak off into the formation. As this occurs, the induced fractures close on the injected proppants, and a conductive channel for hydrocarbon flow remains. One key parameter used in evaluating the quality of the fracturing treatment is called fracture conductivity, which is defined as the product of fracture permeability and fracture width. Over the years, various types of proppants, fracturing fluids, additives, and operational procedures have been developed in efforts to increase fracture conductivity (Zhang, 2014).

### **1.2.2 Laboratory Measurement of Fracture Conductivity**

Laboratory experiments on core samples serve as a direct, controllable, and repeatable approach to study fracture conductivity. There are two types of laboratory procedures for the measuring conductivity: the standard ISO conductivity test and the modified ISO conductivity test. The ISO 13503-5:2006(E) was developed to establish standard procedures and experimental conditions to evaluate conductivity of proppants under laboratory conditions. The standard ISO procedures and apparatus are designed for the purpose of proppant material studies. In contrast, the modified ISO test, or non-ISO standard test, can be utilized for a variety of applications. The modified API conductivity cell accommodates up to 3 times thicker samples to account for fluid leak off through the sample during the experiment. Additionally, rather than flowing 2% KCl through the fracture (as specified by ISO standards), the modified tests can utilize dry gas, wet gas, fresh water, brine of various concentrations and multi-phase flow for different reasons, such as attempting to preserve the shale sample by flowing dry nitrogen (Zhang, 2014).

**Error! Reference source not found.** below shows a schematic of the modified apparatus u

utilized in laboratory fracture conductivity sample testing. The workflow for conducting these experiments is described in *Creation and Impairments of Hydraulic Fracture Conductivity in Shale Formations* (Zhang, 2014).

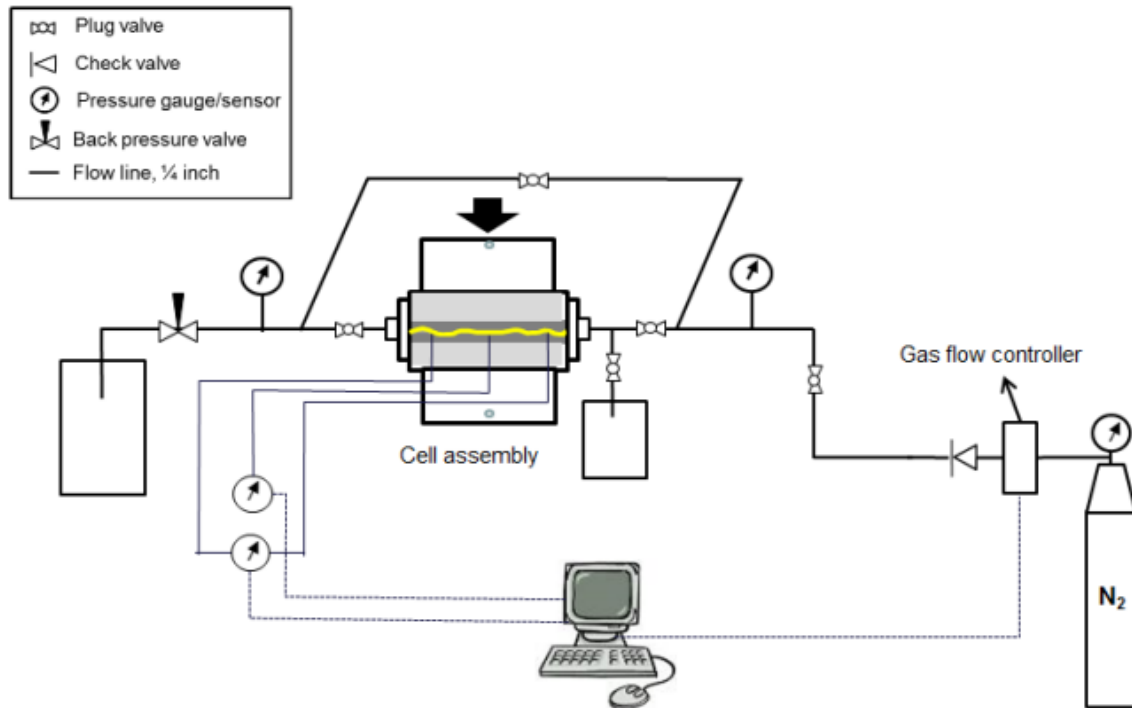


Figure 1.1: Schematic of the experimental setup for conductivity measurement (Zhang, 2014).

Numerous investigations have been conducted over the years that explore a variety of parameters thought to influence fracture conductivity. One study by Guerra, Zhu, & Hill (2017) compared the effects of clay content on fracture conductivity of the Eagle Ford Shale and Marcellus Shale Formations. The authors found that surface mechanical properties and topography can greatly influence fracture conductivity. In Guerra's laboratory experiments, downhole core samples of the Eagle Ford Shale possessing rough

fracture surfaces were used in modified ISO conductivity tests. These core samples were heavily jagged and segmented along the fracture (Figure 1.2), with several abrupt height changes. These abrupt height changes or “steps” were an artifact of the downhole core itself and the subsequent fracture creation. A significant variation of surface area across the test samples was observed, which resulted in some samples having a longer or more tortuous flow path compared to others. The fracture conductivity test samples from the downhole cores represented several challenges during fracture creation, resulting in fractures that were at an angle with respect to the length of the test sample, as well as a clear jaggedness across the length (Guerra, Zhu, & Hill, 2017).

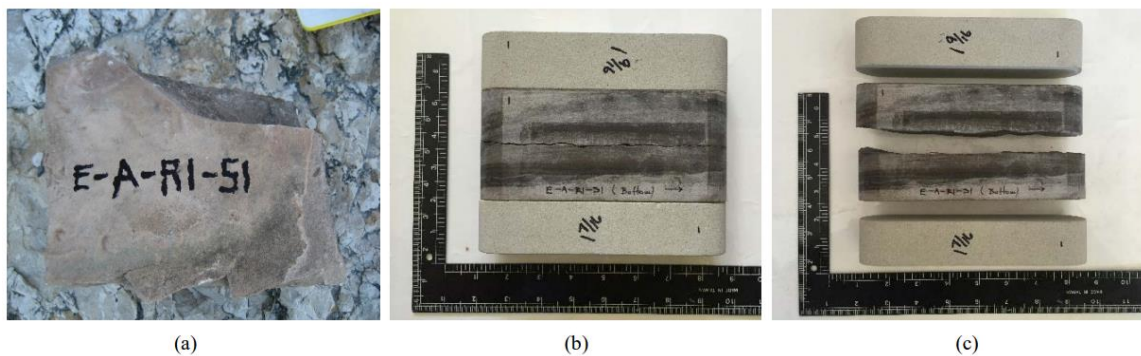


Figure 1.2: Eagle Ford Shale Fracture Conductivity Samples

(a) Outcrop rock sample as collected; (b) Outcrop rock fracture conductivity test sample after fracturing and dimensioning; (c) Test sample in an expanded view (Guerra, Zhu, & Hill, 2017).

One key finding from this study was that fracture surface topography is proportional to fracture conductivity as the closure stress increases. High surface roughness typically correlated with a high initial undamaged fracture conductivity at 1,000 psi closure stress, as shown in Figure 1.3. The surface topography was characterized utilizing the root mean

square (RMS) approach, where the greater the RMS value, the higher the degree of surface roughness.

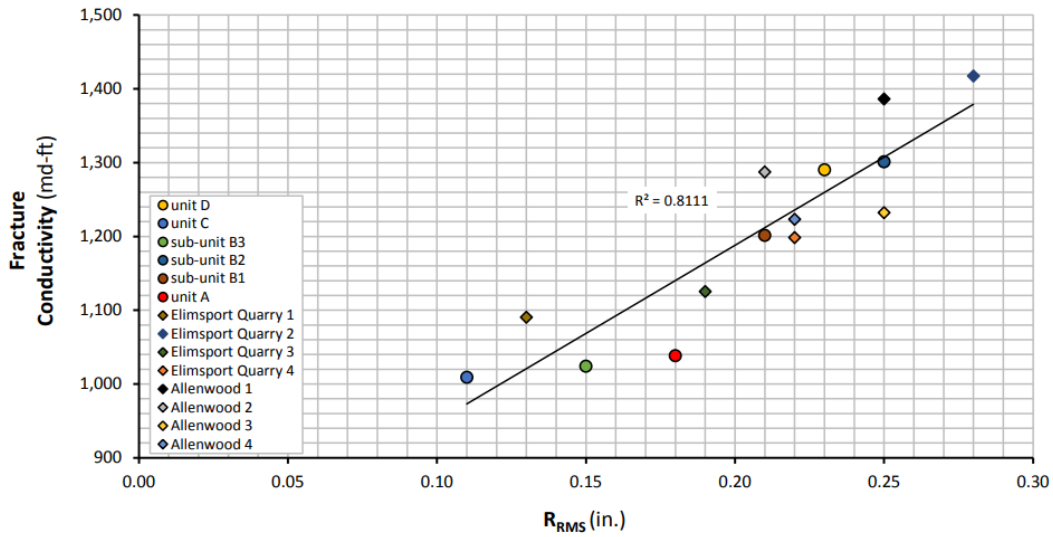


Figure 1.3: Fracture conductivity vs. fracture surface roughness for Nitrogen at 1,000 psi closure stress (Adapted from Guerra, Zhu, & Hill, 2017).

In contrast, the maximum height difference showed an inverse relationship, in which lower maximum height difference on the fracture surface resulted in higher undamaged fracture conductivity values at 4,000 psi closure stress, as shown in Figure 1.4.



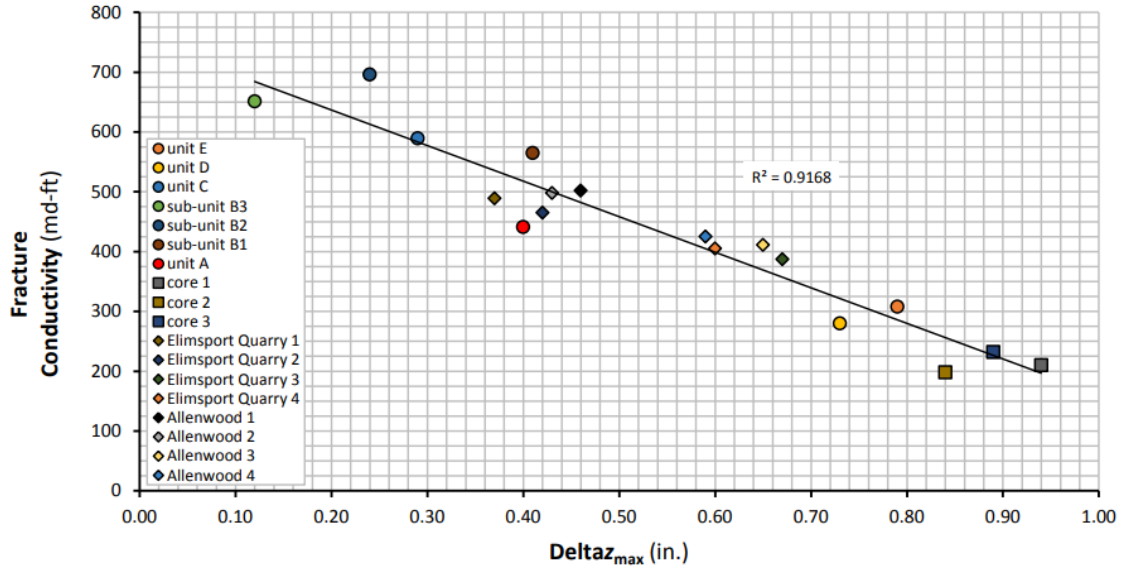


Figure 1.4: Fracture conductivity vs. fracture surface maximum height difference, dry nitrogen flow at 4,000 psi closure stress (Adapted from Guerra, Zhu, & Hill, 2017).

### 1.2.3 Transport of Proppant in Hydraulic Fractures

The placement of proppant in hydraulic fractures is crucial for maintaining a high-permeability pathway for hydrocarbon production, as the presence of proppants is what maintains the fracture opening once the injection fluid leaks off into the reservoir. Fractures may receive varying concentrations of proppant or may have regions of high proppant concentration in the lower parts of the fractures due to proppant settling and dune formation (Warpinski, 2009). In planar fractures, proppants tend to accumulate at the bottom of the fracture until an equilibrium height is reached via fluidization and sedimentation. In contrast, for complex fracture networks and geometries such as rough surfaces, pillars, pinch points, and void spaces lead proppants to become lodged within irregularities, potentially providing increased fracture conductivity (Palisch, Duenckel, Chapman, Woolfolk, & Vincent, 2010).

Previous experimental investigations have been performed to identify the factors that influence proppant transport behavior during the hydraulic fracturing process. Kern et al. (1959) conducted some of the earliest work on slot-flow experiments by use of regular water for the carrying fluid, sand for proppant, and acrylic glass sheets to make a 22-in.-long and 0.25-in.-wide fracture slot. Figure 1.5 below shows a schematic of the equipment used in this study, which focused primarily on investigating equilibrium velocities (the velocity where the height of the settled bed ceases to change) (Kern, Perkins, & Wyant, 1959).

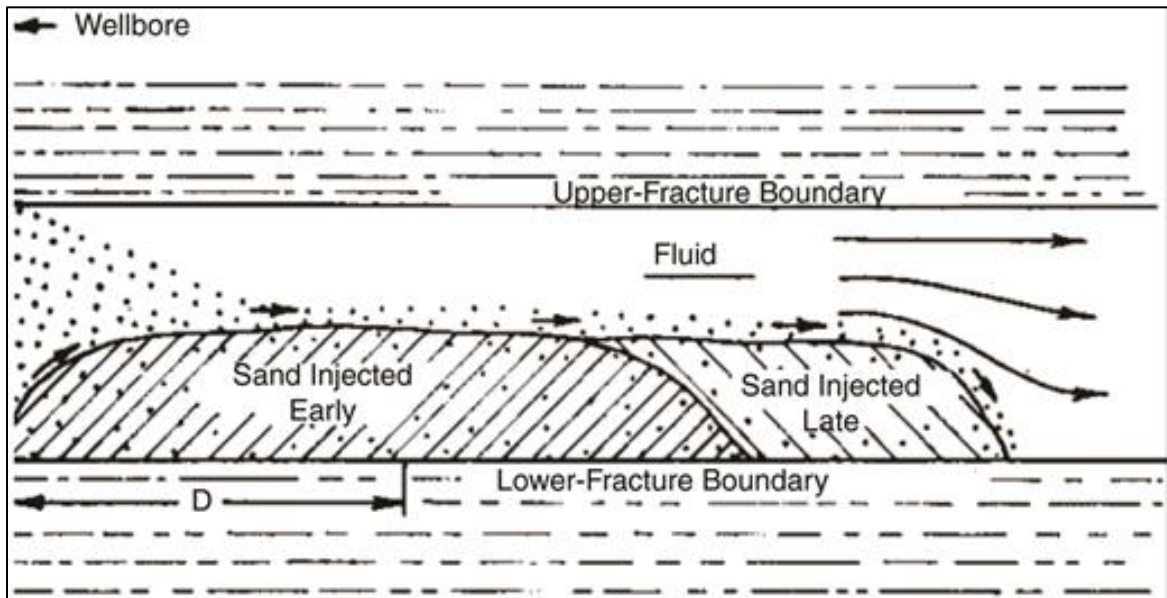


Figure 1.5: Settling of sand injected in a fracture slot (Adapted from Kern, Perkins, & Wyant, 1959).

Kern concluded that proppant has an immediate settling tendency after it flows inside the fracture slot. This settled sand begins to form a dune that becomes larger with time until

reaching a constant height, at which point any additional injected proppant travels further into the fracture (Kern, Perkins, & Wyant, 1959).

A more recent experimental investigation by Bahri & Miskimins (2021) examined the impact of complex fracture geometries on proppant placement. The study utilized an array of acrylic panels submerged in a large water tank to represent a fracture network with a primary, secondary, and tertiary fracture (illustrated in Figure 1.6). The authors concluded that both increasing proppant concentrations and injection rates have a positive impact on proppant transport, with more proppants being transported farther into the slot system in both cases. The higher the proppant concentration, the sooner the equilibrium dune height. Additionally, the authors found that increasing the injection rate led to improving proppant transport by increasing the drag and lift forces on the proppant, which lead to decreased proppant settling velocities and transport farther into the slots (Bahri & Miskimins, 2021).

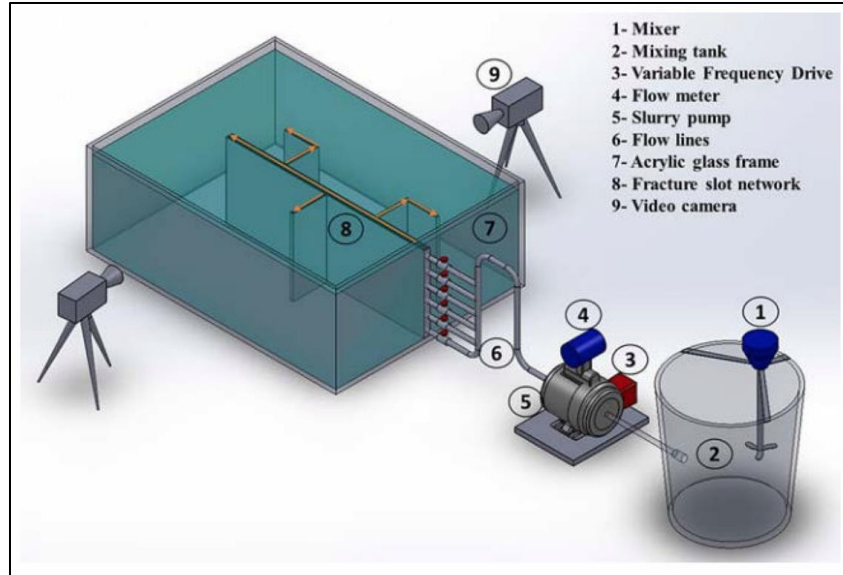


Figure 1.6: Experimental Proppant Transport Apparatus for Complex Slot Systems (Adapted from Bahri & Miskimins, 2021).

#### 1.2.4 Acid Fracture Conductivity

The methodologies for simulating surface roughness used in this study draw inspiration from existing acid fracturing conductivity literature. Acid fracturing is a stimulation process in which acid is injected above fracture pressure into a formation that contains acid-soluble minerals, typically carbonates or sandstones. The dissolution of formation rock leaves etched fracture faces that create lasting conductivity after fracture closure. In contrast to hydraulic fracturing, there is typically no proppant utilized in acid fracturing. The success of acid fracturing depends on the conductivity created and retained by the undissolved matrix under overburden stress in addition to the length of conductive fracture. To have sufficient conductivity after fracture closure, the fracture face must be non-

uniformly etched by the acid while the strength of the rock is still maintained at high levels to withstand the closure stress (Pournik, Zhu, & Hill, 2009).

Unpropped fracture conductivity calculation has been well studied in acid fracturing where fracture conductivity is created by unevenly etched fracture faces. Conductivity correlations for unpropped rough fractures that will be further explored in this work were derived Mou et al. (2011) and Deng et al. (2012). These correlations utilize three surface parameters to estimate the fracture conductivity: correlation length in the horizontal direction, correlation length in the vertical direction, and the standard deviation of the surface topography. These parameters are how we will describe and generate the surface roughness of artificial samples for this work in later sections.

### **1.2.5 Types of 3D Printing & Prior Uses in Well Stimulation Research**

3D printing is a type of additive manufacturing technology that allows for digital 3D models to be made into physical objects, typically in a layer-by-layer fashion. While 3D printing has existed for decades, widespread use of the technology had previously been sparse due to severe cost-restrictions and limited commercial options. Many of the original patents for 3D printing were filed in the mid-1980s. As these patent protections have begun to lift 20 years later, a variety 3D printing processes and materials have been further refined and developed through competition in consumer markets. Printable materials now range from plastics, metals, glass, ceramic, sand, and biomaterials. (Raney, 2015).

Some commercially available machines have achieved resolutions of 100 nanometers and can print objects as large as vehicles, though there exists a tradeoff between speed, size, and detail. Figure 1.7 below shows the print speed and resolution for several common types of 3D printing. Of the types of 3D printing shown in the figure, the two most commonly available are Fused Deposition Modeling (FDM) & Stereolithography (SLA) printing. While it is possible for FDM 3D printers to produce objects micrometer-range accuracy, the time required to do so increases almost exponentially with model size and would require weeks of print time per object. In contrast, resin 3D printers can produce detailed models with 20-75 micrometer accuracy at a significantly greater pace than FDM 3D printers, with printing times ranging from a few hours to days.

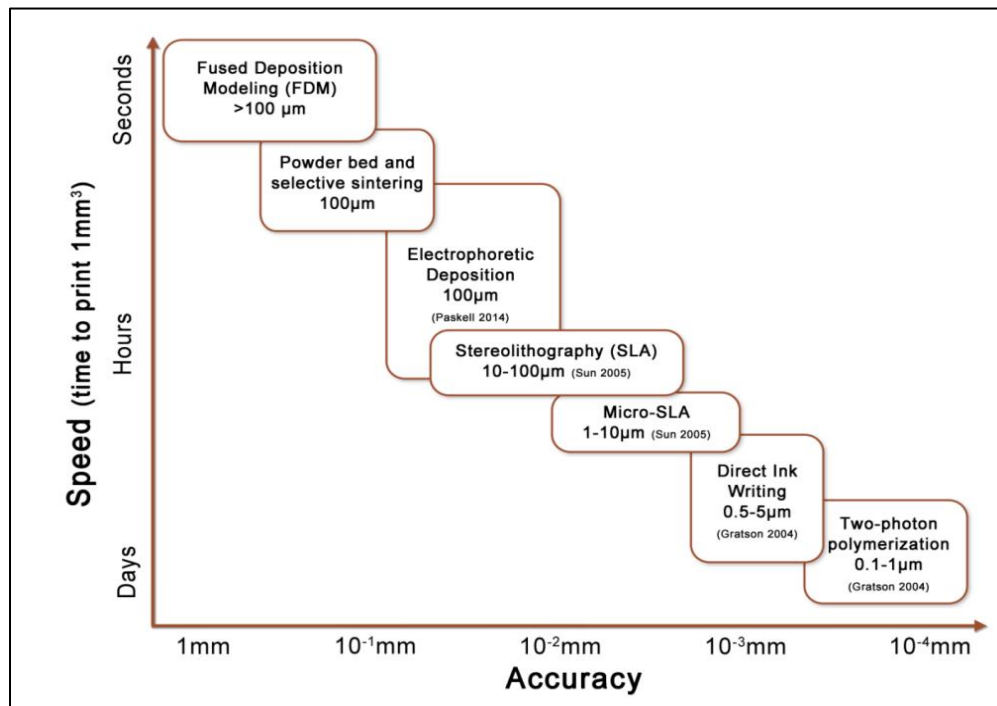


Figure 1.7: Speed vs. Accuracy for common 3D printing techniques (Anderson, 2016)

In the FDM printing process, a thermoplastic is fed into a heated nozzle that brings the material to a semi-melted state (referred to as the glass transition point), where it is deposited onto a build platform. The heated nozzle travels in the X & Y plane to deposit a “slice” of the model onto the platform. Once a layer has been deposited and cooled, the nozzle travels upwards (in the Z direction) before repeating the process to deposit another layer onto previous layer of material. Figure 1.8 shows a schematic of a typical FDM printer, and

Figure 1.9 shows an example of an image taken from the front of a build platform throughout the print process on an actual FDM machine (Olivera, Muralidhara, & Venkatesh, 2016), (Anderson, 2016).

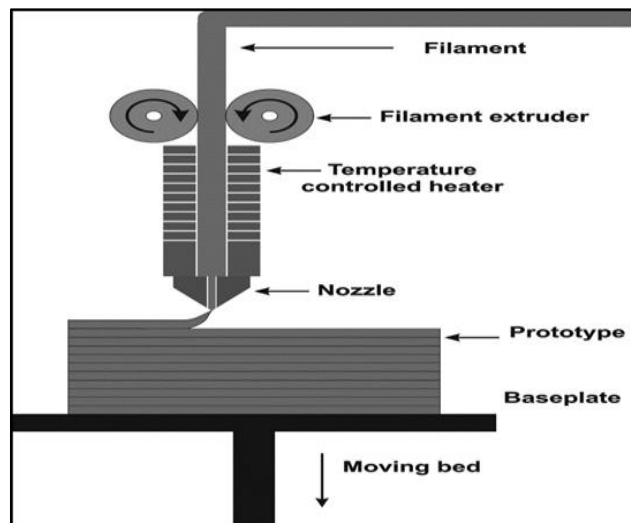


Figure 1.8 : Schematic of a Typical FDM 3D Printer (Olivera, Muralidhara, & Venkatesh, 2016).

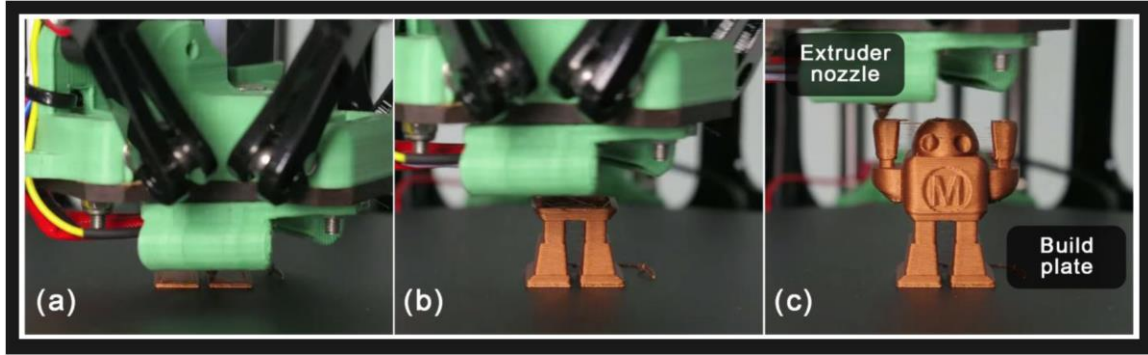


Figure 1.9: Example of fused deposition modeling 3D printing process. (a) Initial empty build plate, (b) partially constructed model, (c) final model. The extruder nozzle extrudes plastic layer-by-layer to build up the final printed object.

Much of the recent literature involving the use of 3D printing in oil and gas experimental research revolves around the use of FDM machines. A 2018 study performed at the Colorado School of Mines aimed to investigate the shear behavior of discontinuous surfaces using artificial cement samples to represent rock. (Isleyen & Duzgun, 2018). This study utilized photogrammetry, a process which involves taking hundreds of high-resolution images to capture 3-dimensional characteristics, was used to digitize real rock samples (**Figure 1.10**) and generate 3D printed replicates (**Figure 1.11**).

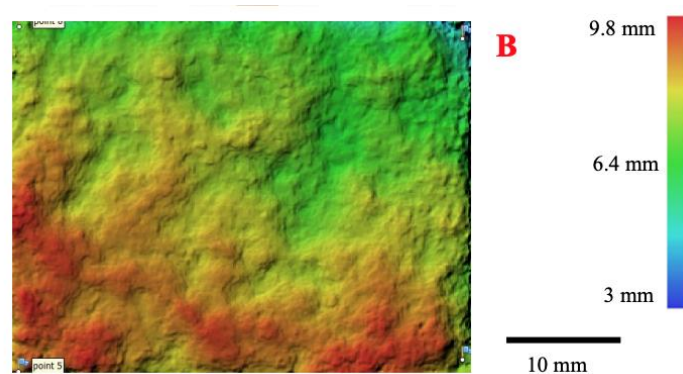


Figure 1.10: Digital elevation model of the natural discontinuity surfaces (Isleyen & Duzgun, 2018).





Figure 1.11: Discontinuity replication procedure (Isleyen & Duzgun, 2018).

The authors successfully demonstrated the use of 3D printing to capture surface roughness characteristics, using the Joint Roughness Coefficient (JRC) as a measurement of both discontinuity and evaluation for the accuracy of the model. Their presented methodology was able to match 79% of the desired roughness (comparing actual JRC to digital JRC), which could possibly be attributed to the resolution of the FDM printer.

A similar study performed by Chinemerem Obi at Texas A&M University also used photogrammetry to recreate digital recreations of rock samples for conductivity experiments. While the 3D printed surface sufficed for recreating replicates capable of being tested for conductivity analysis, FDM printed models suffered from the “fingerprinting” (Figure 1.12) layering effect, a result of the printer’s Z resolution (Obi, 2021).

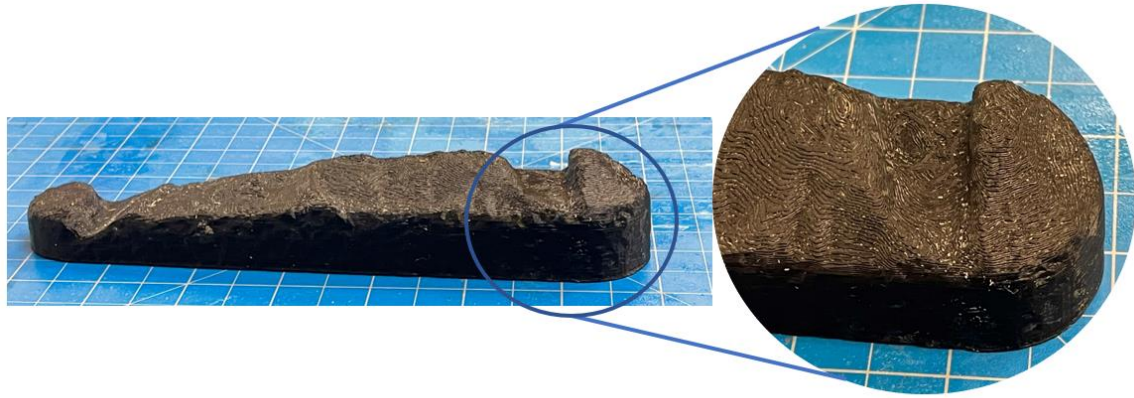


Figure 1.12: Layering of an early FDM Sample (Obi, 2021)

Despite the layering of the model, the author was able to demonstrate a successful workflow for creating replicates for conductivity testing; something that this study aims to continue to refine.

One alternative that offers better resolution compared to traditional FDM 3D printing is the Stereolithography (SLA) 3D printing process. These printers can produce high-resolution prints (commonly in the 25 – 75 micrometer range) in a matter of hours. This 3D printing technology is based on the process of photopolymerization, which refers to the curing of liquid photo-reactive resins (photopolymers) using light in the ultraviolet range of wavelengths (Luongo, et al., 2019). An ultraviolet light source selectively illuminates a photopolymer to produce a solid object with a user-defined shape. below details the typical schematic of an LCD resin 3D printer.

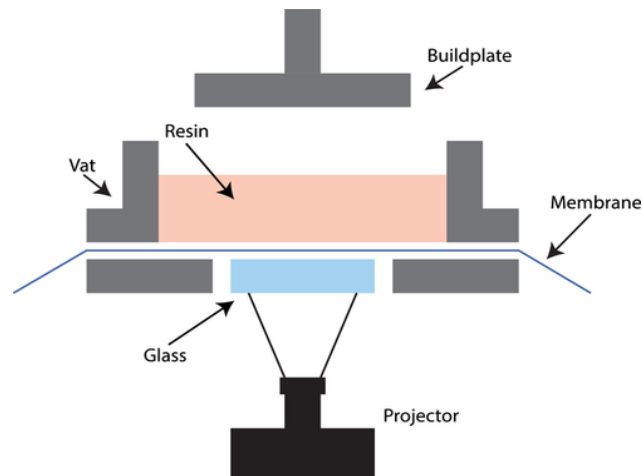


Figure 1.13: Schematic of a standard LCD resin 3D printer (Luongo, et al., 2019)

In the SLA printing process, the build plate begins 1 layer-height (typically 0.05 – 1.15 mm) above the bottom of the clear membrane. The photopolymer is contained inside a vat and at each step a building platform is raised to expose only a thin layer of liquid photopolymer to the projector. The projector then flashes a slice of the image in the UV wavelength onto the build platform for a given amount of time, curing the resin in the shape of the image. The quality of the commercial 3D printers improves continually in terms of the resolution and the complexity of the geometries that can be printed. The resolution of these resin 3D printers is only limited by the pixel resolution of the UV screen.

A few studies have utilized this type of printing before, such as the investigation performed by Timothy Anderson (2016) at Stanford University that utilized SLA printing to generate scaled pore networks. One benefit offered by SLA printing resins is that they offer the ability to be printed transparent, making the printed objects ideal for flow study observations (Figure 1.14). Another benefit of this type of printing is that an entire layer of

the object is cured at once in a matter of seconds, whereas in FDM 3D printing the nozzle must travel across each point of a layer to deposit the thermoplastic.

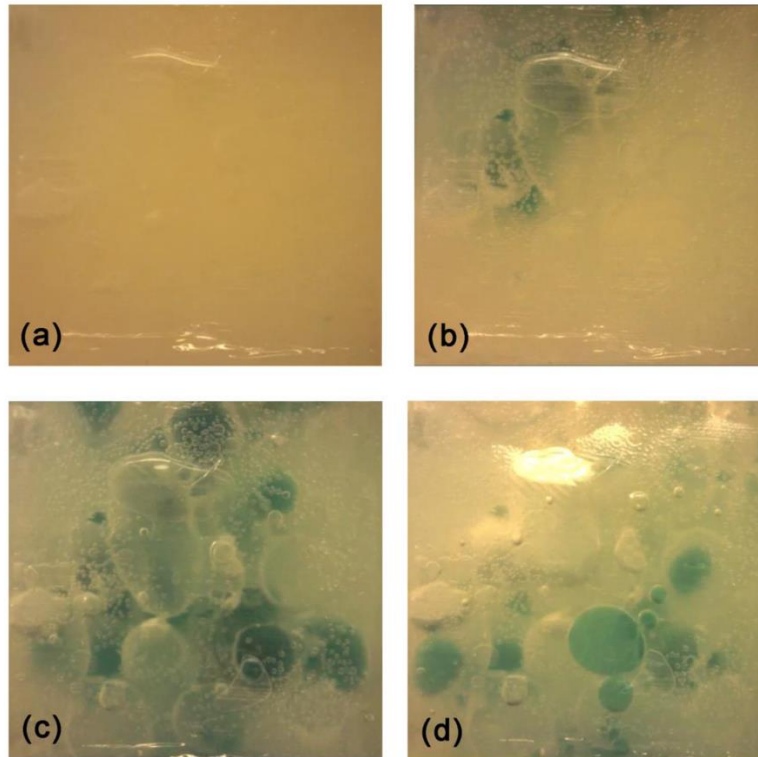


Figure 1.14: 3D printed large-scaled pore network (Anderson, 2016)  
(a) Translucent sample after saturation with canola oil, (b) initial intrusion of dyed ethanol, (c) saturation with dyed ethanol, (d) re-intrusion with canola oil.

To capture and digitize the interior pore geometries of the cores used in this study, the authors utilized a micro-computer tomography (CT) scanning device. While this approach allows the user to visualize the subsurface features of a sample, the technology is limited by the size and / or resolution of the scanning device. The size of the samples used in this study measured only a few inches in dimensions due to both the available sizes of the scanned medium and the limited capabilities of the resin 3D printer (Anderson, 2016). It is

only in the past two years that large resin 3D printers have become readily available on the market.

### **1.3 Problem Description, Objectives and Significance**

There are two key limitations in traditional well stimulation research that this work addresses. The first limitation is that core samples, even when obtained from the same source, can possess a large variability in surface roughness and features due to the inherent irregular nature of fractures. This makes the task of isolating and identifying key variables difficult when no two samples are exactly alike.

Additionally, nearly all historical laboratory studies of proppant transport have utilized flat acrylic panels to represent the fracture walls, whereas rough fracture walls are likely to affect the proppant transport process. It is with these motivations that we propose a workflow to utilize 3D printing to achieve the following objectives:

- 1) To generate digital models of realistic rough fracture surfaces through simulation in a manner that allows the user to control the degree of roughness
- 2) Create physical samples of these models using modern SLA 3D printing with both accuracy and precision in a process that is easily repeatable.
- 3) Provide and execute a standard procedure for post-processing these printed samples so that they are suitable for use in laboratory experiments.
- 4) Demonstrate the successful application of this workflow in both proppant transport and conductivity studies.

The resulting workflow establishes a foundation for future works to leverage 3D printing in additional studies to elevate our understanding of the hydraulic fracturing processes.

#### **1.4 Dissertation Outline**

Chapter I provides the background for the inspiration of this research by reviewing the literature before proposing the objectives. The importance of fracture conductivity and proppant placement on long term well production in shale reservoirs is also discussed, as well as historical examples of utilizing 3D printing in oil and gas research.

Chapter II introduces the workflow and methodology, experimental design, setup, material preparation and general operational procedures. Additionally, this chapter includes the actions we take to mitigate the possibility potential print failures.

Chapter III focuses on the quality of both the printed and cast samples produced. Preliminary results from early experiments are also shown to demonstrate the effectiveness of the workflow.

Chapter IV summarizes the conclusions and key findings of this study and discusses opportunities for continued future research.

## 2. EXPERIMENTAL DESIGN AND PROCEDURE

### 2.1 Introduction

This chapter presents the experimental design, laboratory setup, material preparation, and the procedural challenges. More importantly, this chapter highlights the key experimental design considerations and the actions we take to control the experimental errors.

### 2.2 Workflow for Generating 3D Models

Before 3D printing can begin, a digital model must first be created. In this work, “model” refers to a digital object, whereas the term “sample” is used to refer to a physical object, i.e., one that has been 3D printed and/or cast. The flow chart presented below summarize the workflow for producing 3D printed samples:

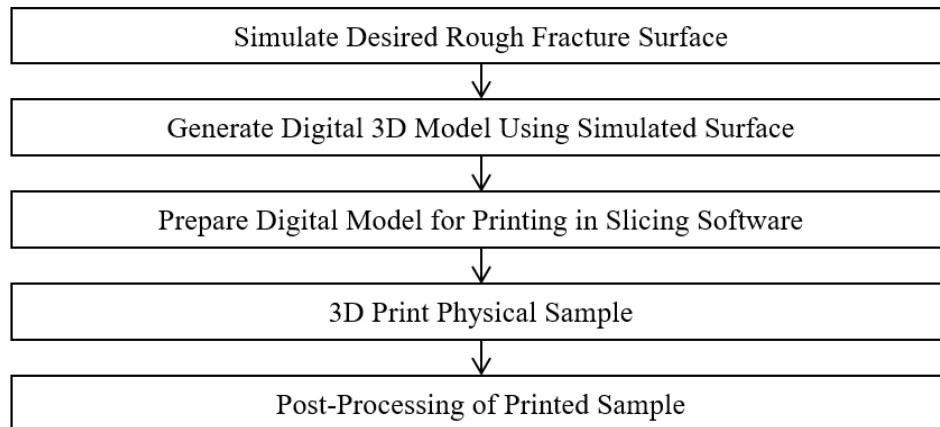


Figure 2.1: Workflow for Producing 3D Printed Samples

Each of the points mentioned in the chart above are discussed thoroughly in the following sections.

### 2.2.1 Capturing Fracture Surface Roughness

Surface characterization has two goals: to provide ways to quantify the spatial relationships of the surface, and to supply parameters for modeling the surface. Several methods can be used to quantify spatial relationships. In this work, the distribution of surface roughness is characterized with the correlation length in the X & Y directions. Correlation length is defined as the distance from a point beyond which there is no further correlation of a physical property associated with that point (Mou, Zhu, & Hill, 2010). This value is calculated by taking the covariance between two variables and dividing by the product of the standard deviation of each variable (Kelkar, 2002). The higher the correlation length, the greater the correlation between a point and neighboring data points. The only inputs needed to fully describe and simulate a surface distribution utilizing GSLIB are the mean, standard deviation, and correlation length in the X & Y direction. To make the correlation length comparable between simulations, the dimensionless correlation length is used to normalize the correlation length by the total length of the simulated sample. These are defined as

$$\lambda_{D,x} = \lambda_x/L \quad (1)$$

and

$$\lambda_{D,y} = \lambda_y/H \quad (2)$$

Where  $\lambda_D$  denotes the respective dimensionless correlation length and  $\lambda_x$  and  $\lambda_y$  are the correlation length in the X & Y directions (Mou J. , 2009). With these few parameters, we can fully describe the roughness characteristics of a fracture surface.






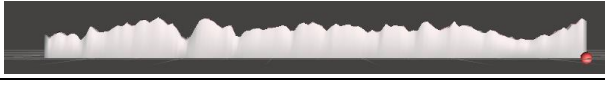
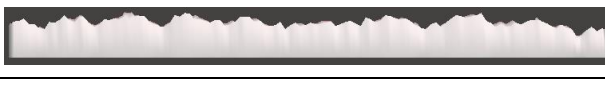

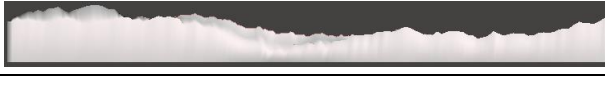
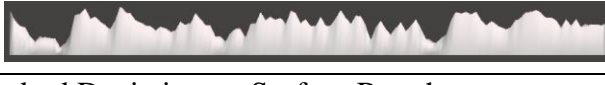
$\sigma$ (in)	$\lambda_{Dx}$	$\lambda_{Dy}$	Side View (Axis)	Model
0.05	0.5	0.5	X	
			Y	
0.05	0.5	0.05	X	
			Y	
0.05	0.05	0.05	X	
			Y	
0.1	0.5	0.05	X	
			Y	

Figure 2.2: Impact of Correlation Length & Standard Deviation on Surface Roughness

The figure above demonstrates that a larger standard deviation in surface roughness is characterized by larger variations in height along the entire model, whereas changes in X & Y correlation length more heavily influence localized variations in height from one point to a neighboring point.

### 2.2.2 Simulating Artificial Fracture Surfaces

The following figures serve as a visualization of how varying degrees of correlation lengths in the X & Y direction for a high-resolution small-scale model. The mean height and standard deviation of each of the simulations is 0.3 inches and 0.05 inches, respectively. Figure 2.3: Simulated 6 X 6 in. surface with  $\mu = 0.3$  in,  $\sigma = 0.05$  in,  $\lambda_{Dx} = \lambda_{Dy} = 0.5$  Figure 2.3 below shows the simulation of a fracture surface with a large dimensionless correlation length of 0.5 both the X & Y directions, while Figure 2.4 shows a simulation with a high degree of correlation in the X direction and a low degree of correlation in the Y direction ( $\lambda_{Dy} = 0.05$ ). Figure 2.5 shows a simulated case possessing a low dimensionless correlation length in both directions (0.05 for X & Y).

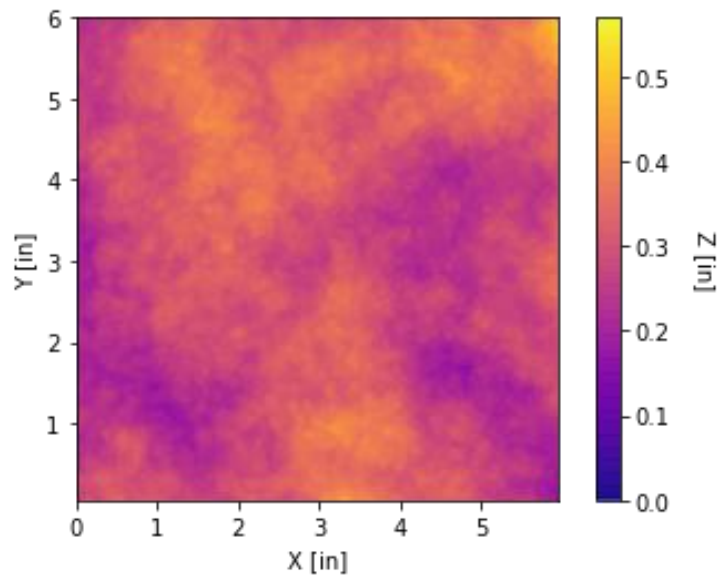


Figure 2.3: Simulated 6 X 6 in. surface with  $\mu = 0.3$  in,  $\sigma = 0.05$  in,  $\lambda_{Dx} = \lambda_{Dy} = 0.5$

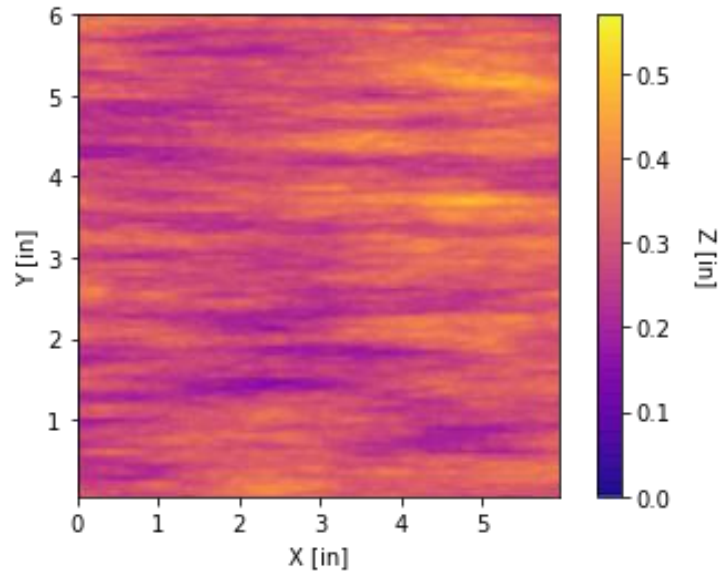


Figure 2.4: Simulated 6 X 6 in. surface with  $\mu = 0.3$  in,  $\sigma = 0.05$  in,  $\lambda_{Dx} = 0.5$ ,  $\lambda_{Dy} = 0.05$

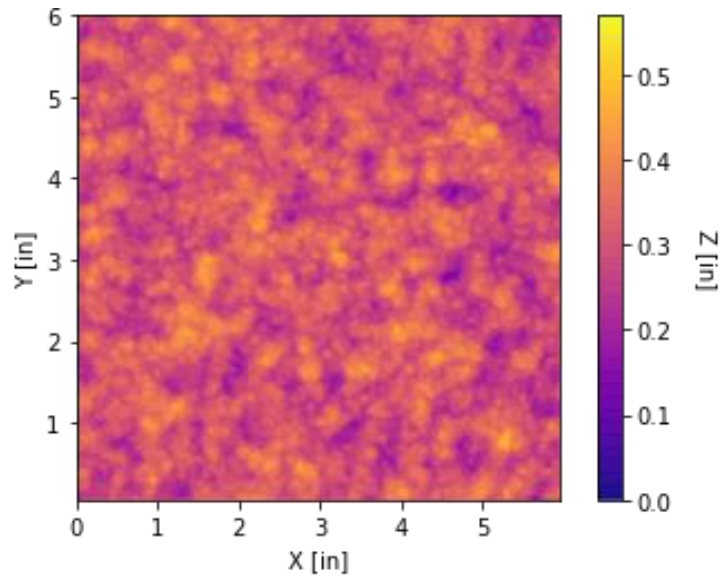


Figure 2.5: Simulated 6 X 6 in. surface with  $\mu = 0.3$  in,  $\sigma = 0.05$  in,  $\lambda_{Dx} = 0.05$ ,  $\lambda_{Dy} = 0.05$

Increasing the mean height input parameter for the simulation will serve only to increase the thickness of the final model, not the variation in surface height. We can exaggerate the variations in each simulation by changing the standard deviation. Figure 2.6 below demonstrates this by maintaining the X & Y correlation length from Figure 2.4, but with a standard deviation of 0.1 inches instead of 0.05 inches.

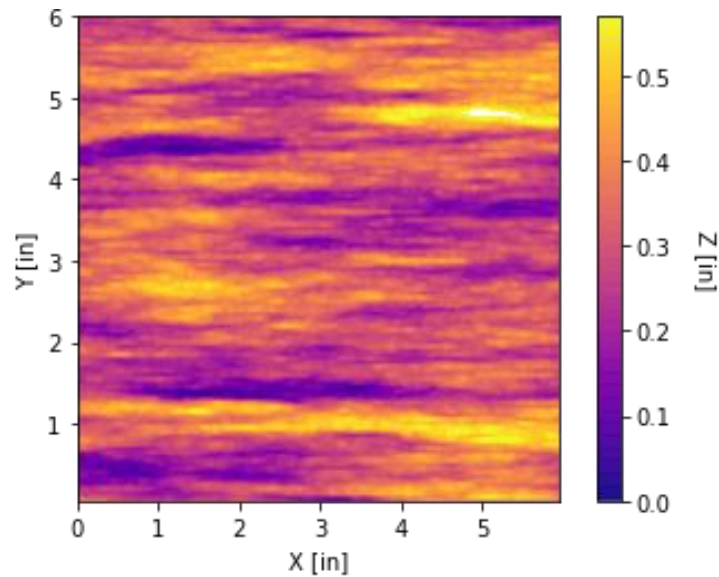


Figure 2.6: 0.5 Simulated 6 X 6 in. surface with  $\mu = 0.3$  in,  $\sigma = 0.1$  in,  $\lambda_{Dx} = 0.5$ ,  $\lambda_{Dy} = 0.05$

### 2.2.3 Creating a Digital Fracture Model

The simulation output described in the previous section consists of a set of X, Y, & Z points generated at a specified interval (in this work, 0.01 inches). To generate a digital model, these data points are used to generate a 3D “mesh” in the form of a .STL file, which is an amalgamation of small triangles that fully describe a surface. To generate a surface of triangles, the data points generated from the simulation are joined into groups of 3 and

assigned a calculated normal vector to notate the direction of the surface. To illustrate this concept, the figure below shows a magnified view of one of the completed fracture surface models.

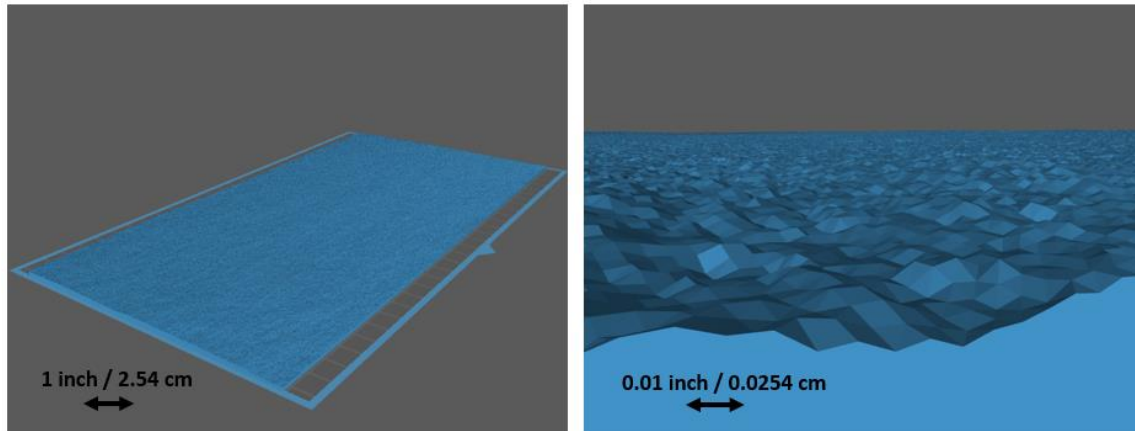


Figure 2.7: A digital model of a fracture surface (Left) and a magnified view of the triangulated surface (Right)

The close-up image shown in Figure 1.1Figure 2.7 demonstrates how the digital model consists of these triangulated surfaces which were generated from the X, Y, & Z data points output from the simulation. The higher the density of data points, the greater computational time required for the entire model. Through trial and error, a data point resolution of 0.01 inches was found to be ideal for maintaining a reasonable computation time without sacrificing surface detail. At this resolution, over 500-million triangles are used to describe a single model.

### 2.3 3D Printing Workflow

This section serves to detail the steps to follow for utilizing the 3D printer after the model has been acquired. The model must first be prepared in a slicing software, which converts

the model into a set of instructions interpreted by the 3D printer. Next, the printer must be calibrated and prepared for printing prior to uploading the model. Additional troubleshooting steps for common errors encountered in 3D printing are also discussed.

### 2.3.1 Description of Printer Apparatus

The printer apparatus consists of multiple components used in sync to create a physical 3D sample. Figure 2.8 below details the major components of the resin 3D printer referenced in the procedures:

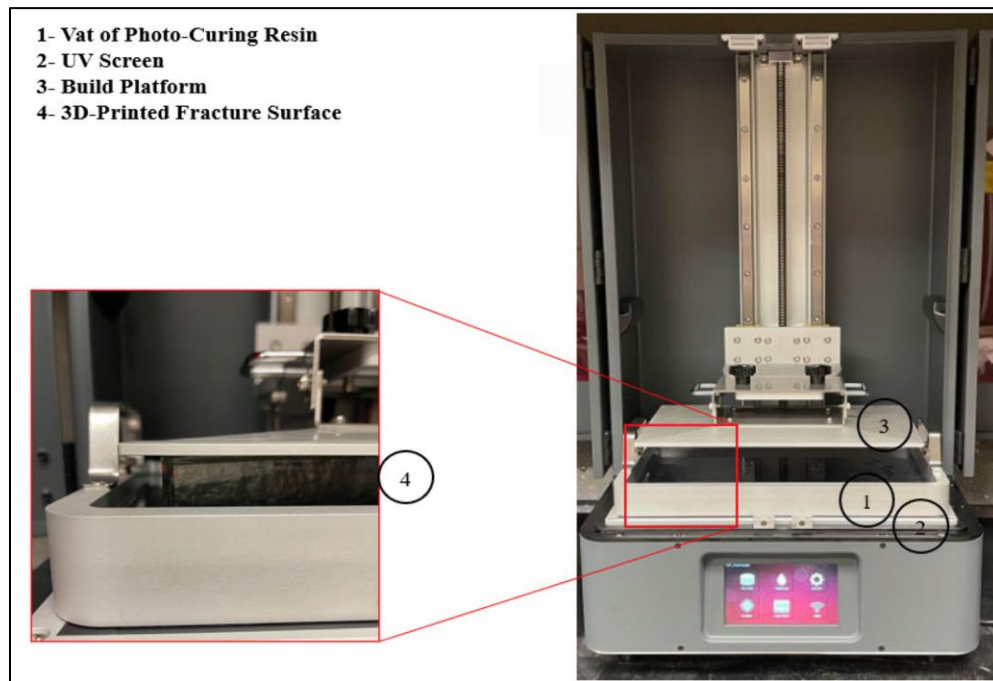


Figure 2.8: Description of Printer Apparatus

For a resin 3D printer, the bottom of the vat is made of a transparent plastic sheet that allows UV light from the screen below it to penetrate into the resin, curing it to the build platform.

### 2.3.2 Preparing a Digital Model for Printing

Once the 3D model has been generated, the model must be pre-processed in a slicing software that converts the object into a set of instructions for the printer to follow. The slicing software allows the user to control parameters such as exposure time, layer height, motor movement speed and positioning, etc. These parameters are further defined in the appendix. The term “slicing” is used to describe this process as the model is divided into thousands of 2-dimensional images in the vertical direction. These images are then projected onto the build platform to selectively cure the resin in the shape of the image.

The slicing program used in this study was an open-source software called Chitubox. The Chitubox workflow is specifically designed to prepare .STL files into a set of instructions for resin 3D printers and includes functions for controlling model orientation and important printer parameters. The procedure for slicing the .STL file in Chitubox is as follows:

- 1) Click “Open File” and select the desired .STL file
- 2) Orient the model to where it fits onto the build platform with minimal unsupported overhangs. In the case of these fracture surfaces that measure 12 inches in length and width, the models must be slightly angled to fit onto the 11.5 inch-length of the printer volume.
- 3) Open “Settings” and ensure that the correct machine is defined on the left of the user interface. The machine used in this study is the Phrozen Transform; therefore, the values described below in Figure 2.9 should be utilized. These parameters are

unique to this printer model and should not be adjusted, as they define the X, Y, & Z build volume of the machine for the slicing software to prepare the model.

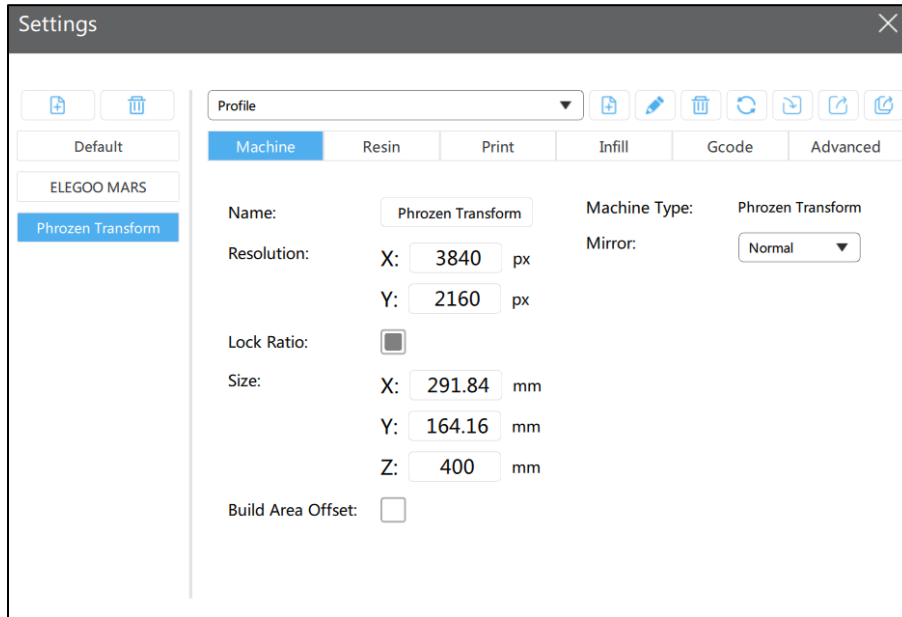


Figure 2.9: Standard Resolution Settings for the Phrozen Transform 3D Printer

- 4) Click the “Print” subheading to open the settings that control the motion and exposure time during the print. The key settings listed here are:
  - a. Bottom Layer Count:
  - b. Exposure Time
  - c. Bottom Exposure Time
  - d. Lifting Distance
  - e. Bottom Lift Speed
  - f. Lifting Speed
  - g. Retract Speed

These settings are described in further detail in the appendix.



- 5) These parameters will vary from resin to resin and must be calibrated to determine the optimum settings for each material. The figure below details the optimal conditions found for printing the transparent resin utilized in this work.

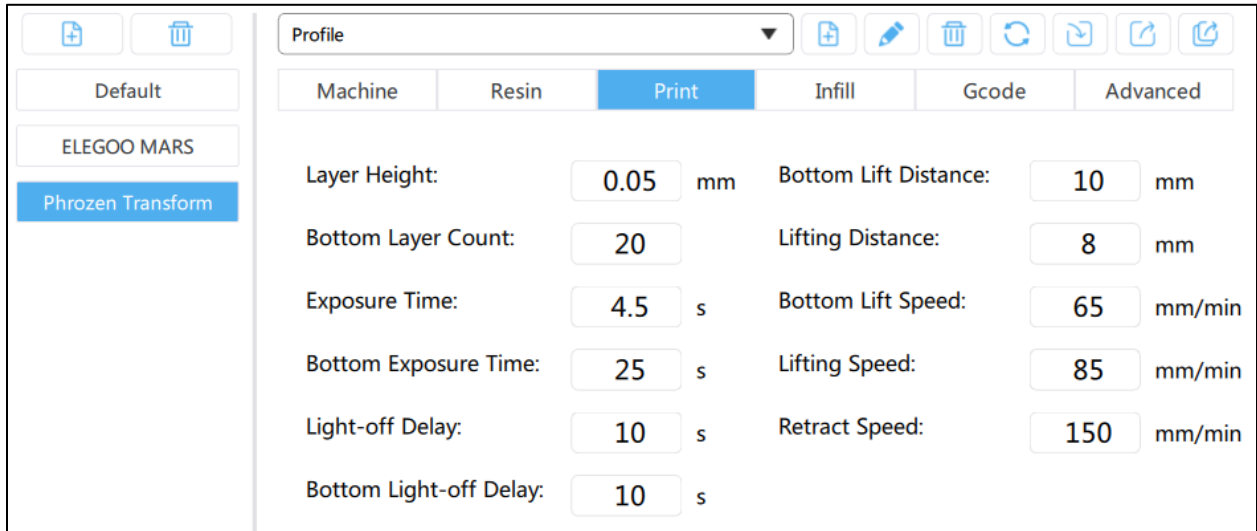


Figure 2.10: Optimal Settings for Transparent Resin on the Phrozen Transform Printer

- 6) Once these values have been properly adjusted, exit the settings menu, and click “Slice.” The software will then begin to generate the instructions for the printer. Some larger detailed models may require up to several hours of slicing time as the program slices the model into 2D pixelated images.
- 7) After the model has been sliced, a preview will appear that shows how many layers the print will have, as well as the image that will be projected onto the resin for each layer, as shown in Figure 2.11 below. The estimated volume and completion time of the model is also displayed.

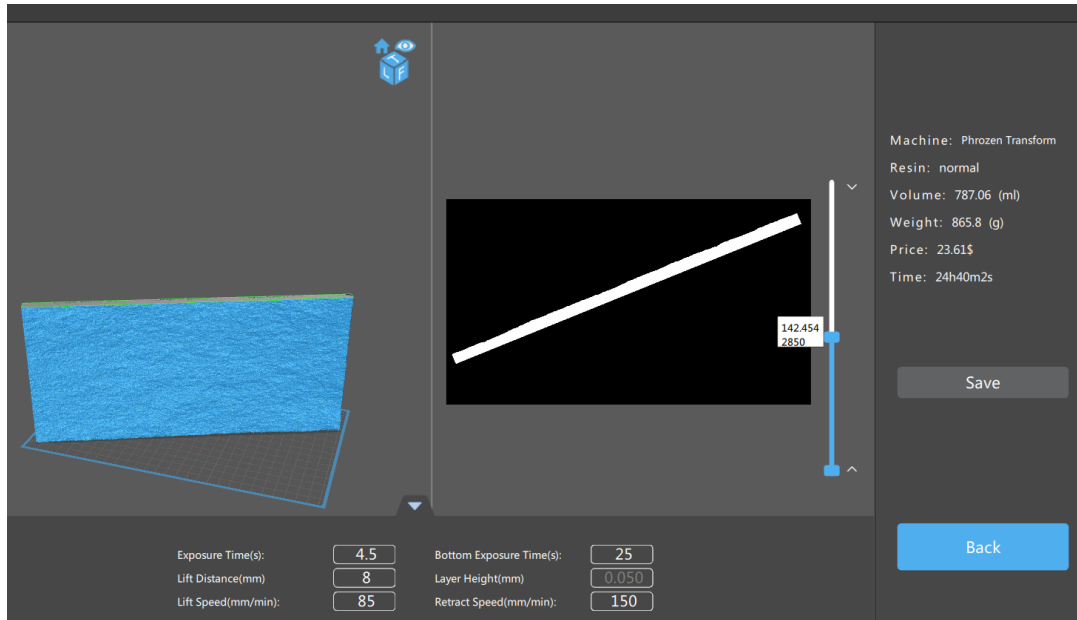


Figure 2.11: Preview Generated from Slicing Software

- 8) Click “Save” and save the model to a removable USB drive. The file will save in the form of a .zip file.
- 9) Once the .zip file has been uploaded to the removable drive, change the file extension from a .zip to a .phz file by either selecting the name and editing the extension directly (for windows users) or by right clicking on the file, selecting “more info,” and changing the extension manually (for mac users). This must be done for the printer to recognize the file.
- 10) After safely ejecting the USB drive, the .phz file can be uploaded to the printer. This process is described in further detail in the next section.

### 2.3.3 Printing & Post-processing Workflow

Once the digital model has been sliced, the model is ready for printing. After inserting the USB containing the print file into the back of the printer, the process for using the printer is as follows:

- 1) Select “Plates” on the home screen of the printer to enter the file import menu.
- 2) Select the “Read from USB” button located in the upper right of the screen.
- 3) Select the desired file and press “Upload.” The file will now be displayed on the “Plates” screen after the import is completed.
- 4) After importing, return to the home screen and select “Plates” again. Select the uploaded file to enter a print preview screen.
- 5) Prior to selecting “Print”, ensure that there is no cured material remaining in the resin tank, which could potentially damage the FEP sheet and the LCD screen.
- 6) After confirming that the print information on the preview screen is correct, press the check button to begin the printing process. The build platform will submerge itself into the vat, and the print will begin.
- 7) If printing large objects, such as the fracture panels, additional resin may need to be added over the course of the print job. The printer should be checked on periodically to ensure that the vat does not run out of resin.
- 8) Once the model is finished printing, loosen the screws on top of the build platform to remove the print and platform from the printer. Take extra care to ensure that uncured resin does not spill onto the printer while transferring the build platform

- with the print attached to a wash station, where the print can be removed with use of a scraper.
- 9) While using the scraper to remove the print from the build platform, apply a light force to the area the print is adhered to the build platform, orienting the tool in a safe manner pointed away from arms and hands.
  - 10) After removing the print, return the build platform to the printer and tighten the screws to secure the platform in place.
  - 11) Remove excess resin from the model by washing it down with isopropyl alcohol under the fume hood. For smaller objects, an ultrasonic cleaner can be utilized for ideal results.
  - 12) After drying the model, place it into the UV curing station for 5-10 minutes per side to allow the model to fully cure.

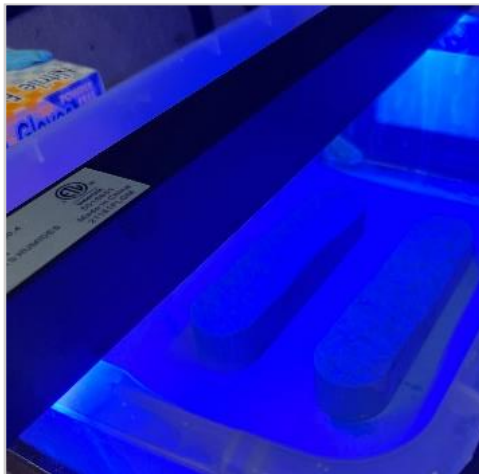


Figure 2.12: 3D Printed Samples Curing under UV Light

13) (Optional): For transparent models, applying a thin coat of UV resistant clear coat will prevent the model from yellowing over time and maintain optimal clarity when dry.

### 2.3.4 Sample Validation with Profilometer

A profilometer is a precision vertical distance measurement device capable of measuring small surface variations in vertical surface topography as a function of position. The vertical measurement is made with a laser displacement sensor while the sample is moved along its length on a moving table. That measurement is repeated several times over the width of the sample to cover the entire surface area. The resolution on the vertical measurement is 0.002 in.; the horizontal X and Y resolution is 0.05 in. The process of utilizing the profilometer for surface scans are similar to that discussed the 2007 workflow described by Camilo Nieto (Nieto, 2007).

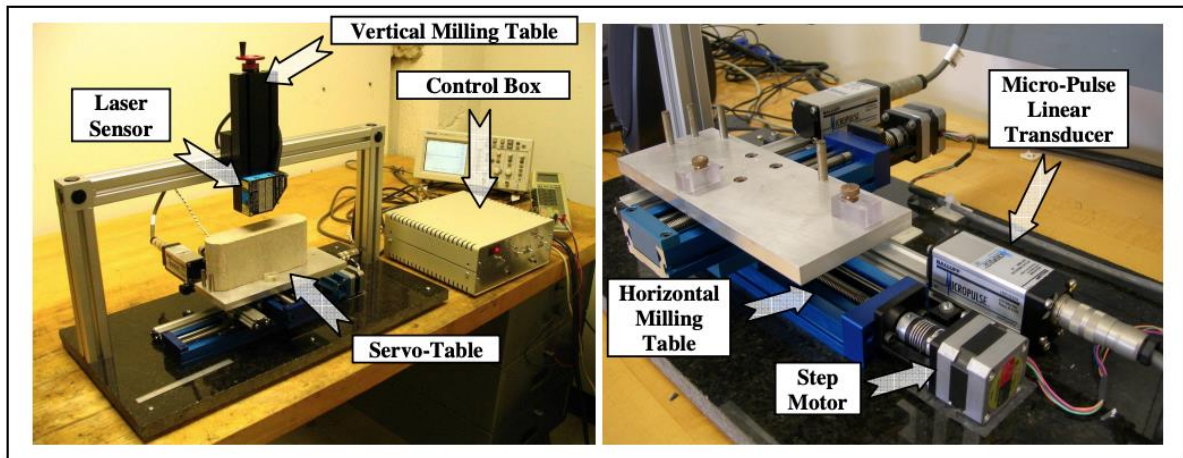


Figure 2.13: Overview of Profilometer Set Up

While the X & Y step-size resolution of the profilometer are 5 times larger than the resolution of the model, the aim of the scans is to obtain a distribution of the Z height values over the surface of the printed sample to verify the height distributions with the digital model.

## 2.4 Fracture Conductivity Sample Design

This section details the process for creating the samples utilized in fracture conductivity experiments. The workflow presented in a previous section resulted in a square .STL file with specific surface characteristics. To transform this shape into a useable cast for a fracture conductivity sample, a digital version of the confining cell was modeled in a CAD software, shown in the figure below.

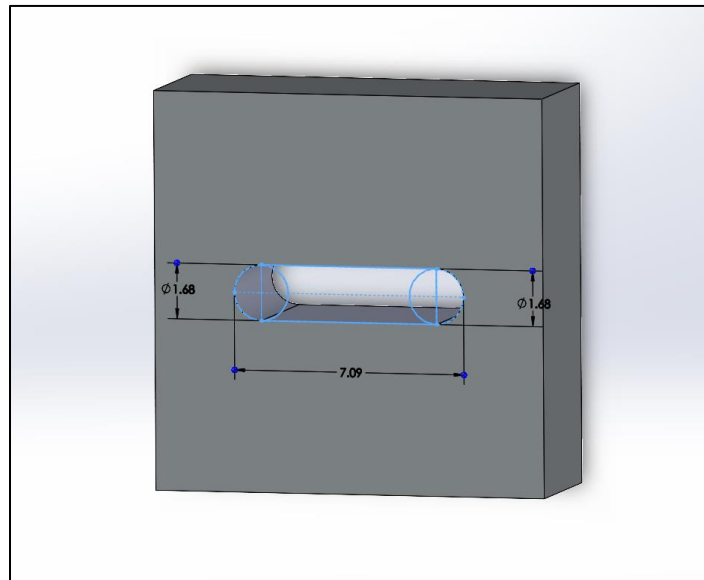


Figure 2.14: Fracture Conductivity Cell

The dimensions of a fracture conductivity sample must fit inside the fracture conductivity testing apparatus; therefore, the digital model must be created with the dimensions of 7” in length, 1.68” in width with circular edges.

Once a digital model of a fracture conductivity model has been created and a physical sample 3D printed, the sample can be cast in cement to generate replicas that can withstand conductivity tests.

#### **2.4.1 Creating a Digital Conductivity Model**

The digital fracture conductivity model can be easily generated by adding one step to the workflow for creating the square fracture surface models described in the previous section. After importing a model of the conductivity confining cell model and the desired fracture surface model, a built-in function within the Chitubox slicing software can be utilized to “subtract” one geometry from the other, removing the intersecting geometries. Listed under the “Edit” tab, the “Boolean Difference” operator allows the user to generate a new model based only on the regions that fail to intersect, leaving behind the desired surface geometry for a conductivity sample, as illustrated in Figure 2.15. The resulting model possesses the surface geometry of a rough fracture surface and the correct outer-dimensions for a fracture conductivity experiment sample.

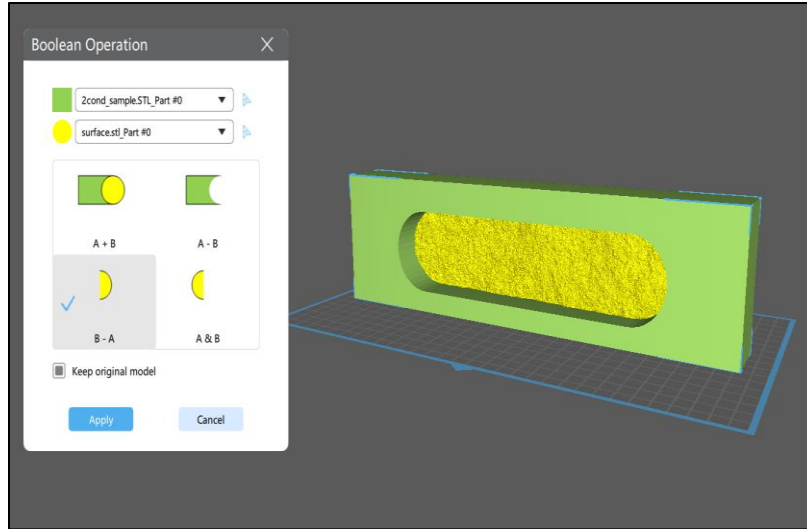


Figure 2.15: Generating Digital Model for Fracture Conductivity Cell Sample

#### 2.4.2 Generating Conductivity Samples from 3D Prints

One limitation of 3D printed materials is that these materials often lack the strength required for destructive tests. In fracture conductivity experiments, samples undergo closure stresses in the range of several thousand PSI, which is far too great for 3D printed materials. Therefore, cement replicas of the 3D printed samples are cast from a silicone rubber mold. One benefit of this approach is that a silicon mold can be re-used to create multiple samples of the same model with ease.

Once a 3D printed conductivity sample had been post-processed (as shown in the previous sections), the sample was then secured to the bottom of a rectangular container with contact adhesive. Then, a two-part silicon casting rubber is poured over the sample and left to cure. Once the mold has finished curing, the 3D printed sample can be removed from the mold, which maintains a negative of the original sample.



## 2.5 Proppant Transport Apparatus Design

The final workflow presented in this study details the process for 3D printing large fracture networks for use in proppant transport experiments. In addition to the developed workflow, a demonstration case utilizing simulated fracture surfaces to generate artificial fracture surfaces is presented.

For use in the creation of fracture surfaces greater than the capable build volume of the resin 3D printer, the full-sized model of the fracture can be split into smaller portions, referred to as “tiles,” and joined together. To demonstrate this, a fracture network consisting of a 4ft × 2 ft main fracture and 1 ft × 2 ft side fracture was modeled for use in proppant transport experiments utilizing the procedures outlined in previous sections. The following figure includes a diagram and rendering of the desired apparatus:

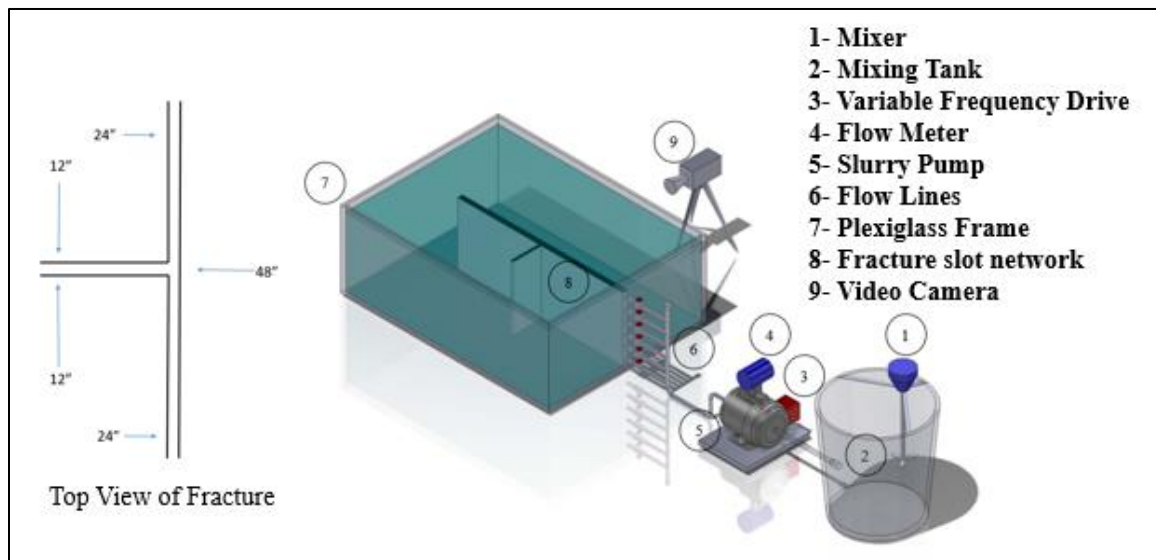


Figure 2.16: Schematic of Proppant Transport Apparatus

The large fracture model was divided into 1ft  $\times$  1 ft tiles with a thickness of 0.25 inches added on to the fracture surface distribution. Each tile was printed and post-processed prior to being assembled into the large fracture apparatus.

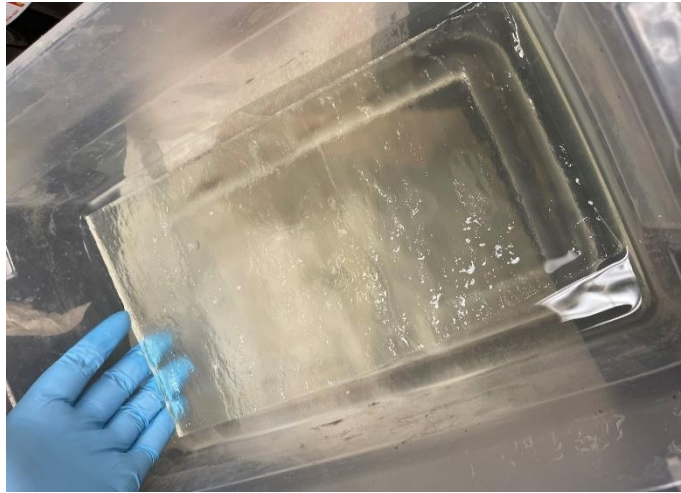


Figure 2.17 : A single fracture panel being post-processed in isopropyl alcohol.

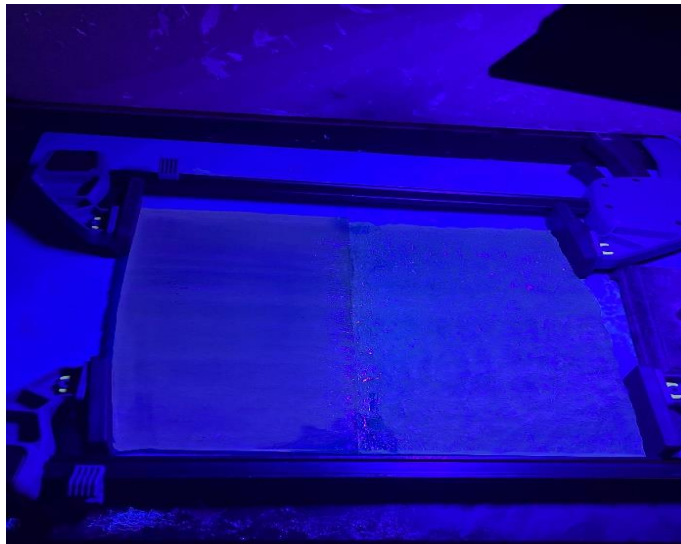


Figure 2.18 : Two fracture panels being joined together with contact adhesive under a UV light.

## 2.6 Key Design Challenges & Considerations

Despite the numerous advantages to the processes outlined above, there are still a few potential challenges that need to be addressed when utilizing resin 3D printing for large-scale objects. The following items must be considered when attempting to print large parts:

1. Large resin prints are subject to potential warping in the event of slight temperature fluctuations. To mitigate this effect, the printer should be kept in a stable-temperature environment. Additionally, to prevent the resin vat from absorbing heat over the duration of the print from the UV light source, a few seconds of time are added between each layer in the slicer settings to allow the UV screen to dissipate heat.
2. Liquid resin poses potential safety hazards to the user when fumes are inhaled, or the material is exposed to skin. Proper PPE including a lab coat, gloves, and safety glasses must be utilized when working with 3D printed resins in the lab. The printer must also be placed under the fume hood to prevent the accumulation of resin fumes.
3. When printing large parts, proper adhesion to the build plate can sometimes be a challenge. Increasing the exposure time of the bottom layers can help prevent the print from becoming separated but increasing the exposure too much can impact the dimensions of these first few layers. Offsetting the print with printed support materials prevents this distortion, but at the cost of print speed. Lastly, one solution that worked well for this challenge was sanding the build plate with 100-grit

sandpaper, increasing the surface area available for the first of the bottom layers and obtaining better adhesion.

4. The qualities of resin materials can vary greatly between products and manufacturers. Several brands and products were tested to optimize the strength and clarity of the models. Even so, in the case of proppant transport experiments, it is difficult to determine how many tests a 3D printed fracture network can withstand prior to the erosion of some surface details.

### 3. RESULTS & DISCUSSION

#### 3.1 Introduction

This chapter discusses the quality of the 3D printed models resulting from the procedures outlined in previous sections. This includes the distribution of surface heights found by the profilometer scans, visual confirmations of model transparency for the 3D printed fracture surfaces, and the assembly/testing of the large rough-walled fracture apparatus.

#### 3.2 Proppant Transport Apparatus

The figure below shows the successful matching of two rough fracture surfaces in transparent resin achieved with 3D printing. From the top-down view of the panels, the samples appear opaque-translucent due to the thickness of the model in this orientation.

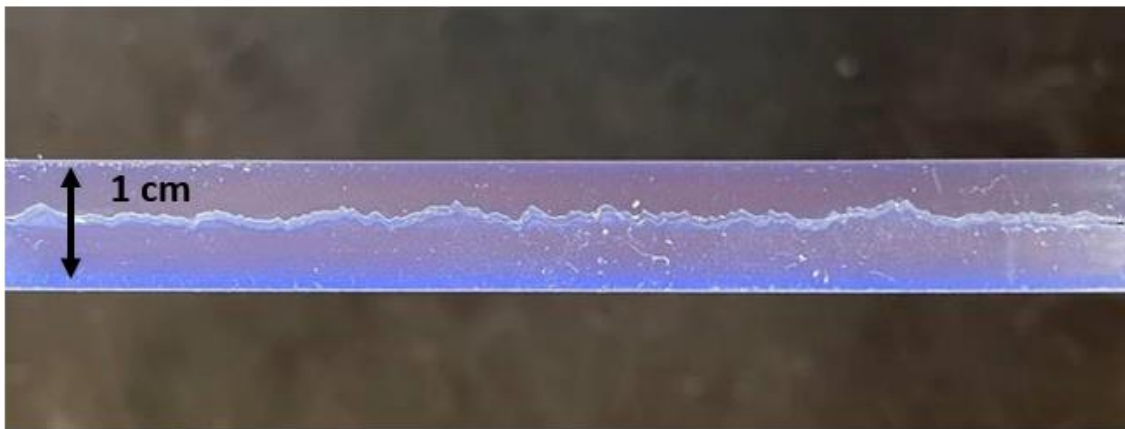


Figure 3.1 : Matching Rough Fracture Surfaces

Observing the panels from the side as shown in Figure 3.2 reveals that a high level of transparency was achieved:

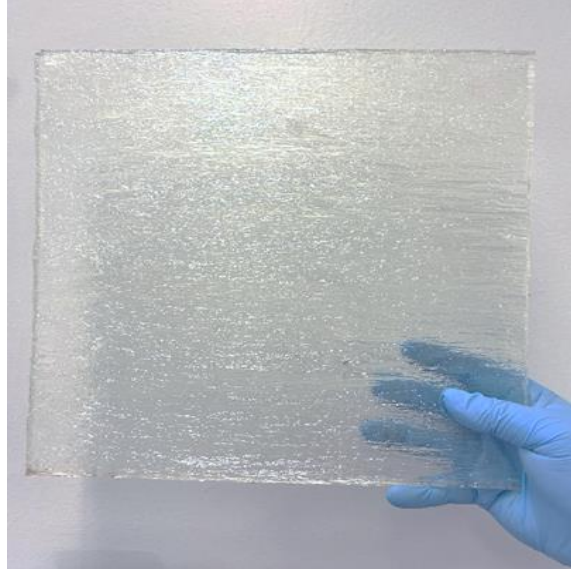


Figure 3.2: Side View of Single 1ft X 1 ft Transparent Fracture Tile

### **3.3 Assembling the Transport Apparatus & Early Experimental Results**

The tiles for the main and side fracture for use in the proppant transport study were printed over the course of two months and assembled at the Colorado School of Mines. While assembling, braces were added along the central joints of the fractures by drilling a hole partway into the depth of the apparatus and bolting in aluminum channel. This was done as a precaution to mitigate any forces experienced by the panels during pumping. Figure 3.3 below shows a view of the completely assembled apparatus.



Figure 3.3 : Final Proppant Transport Apparatus

The braces alongside the sides of the fracture panel serve to prevent any movement of the fracture width while pumping slurry during an experiment. Additionally, the braces along the top and bottom serve to seal the fracture so that the slurry must exit through the ends of either the side fracture or main fracture.



Figure 3.4 : Duning shown from Proppant Transport Experiment

Figure 3.4 above demonstrates how the transparency of the 3D printed fracture surfaces is more than sufficient for observing proppant transport patterns. The proppant was injected into the slot system using the following experimental steps. First, the Plexiglas tank was filled with 50 gallons of tap water until all of the fracture slots were fully submerged. Then the mixing tank was filled with 55 gal of tap water and the appropriate proppant amount was added to the mixing tank (55 lbs. of proppant to achieve 1 PPG, 110 lbs. of proppant to achieve 2 PPG). The slurry was mixed for 10 minutes to obtain a uniform mixture. After mixing, the flow meter was adjusted to the required injection rate of 15 gal/min (equivalent to 40 bpm based on Reynolds number scaling) using the VFD. After the VFD was adjusted, both recording cameras were turned on to record the proppant transport through the fracture slots. Then the valves were opened, and the slurry injected from the tank into the slot system until the supply tank was drained. After the injection was completed and the proppant settled, final measurements were taken and proppant samples were collected from sampling points. The collected proppant samples were then dried in the oven and sieved. All the aforementioned test steps were repeated for each sand concentration (1 PPG & 2 PPG) and size (100-mesh & 40/70 –mesh). The findings from these early proppant transport experiments utilizing 3D printed fracture surfaces are presented in SPE 210196, “Experimental Study of Proppant Transport Using 3D-printed Rough Fracture Surfaces” (Tatman, Bahri, Zhu, Hill, & Miskimins, 2022).

### **3.4 Conductivity Samples**

This section serves to discuss the quality of the printed conductivity samples as well as the quality of the cement replicates generated through casting. Additionally, a comparison



between the modeled surface roughness, printed sample roughness, and cement sample roughness is performed utilizing profilometer scans.

To verify the quality of the 3D printed rough fracture surface, a sample was created using a simulated surface with  $\mu = 0.3$  in,  $\sigma = 0.05$  in,  $\lambda_{Dx} = \lambda_{Dy} = 0.5$  and trimmed to the shape of a standard conductivity sample for profilometer scanning. The figure below shows a side-by-side comparison of the digital model and the 3D printed surface.

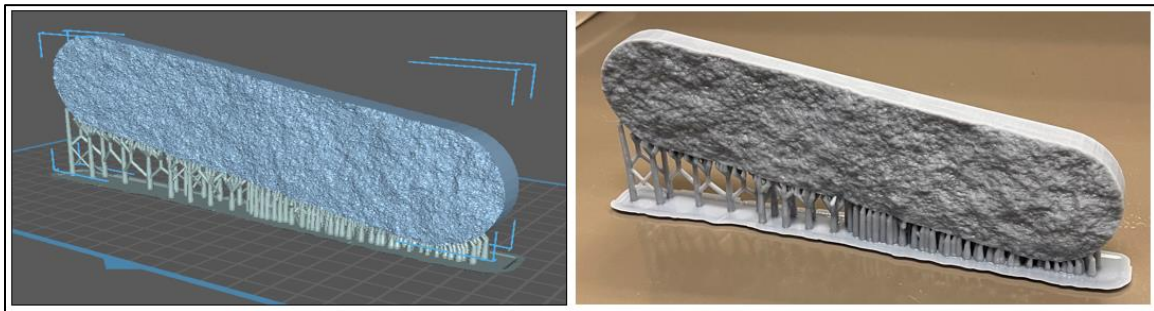


Figure 3.5 : Digital Model (Left) and 3D Printed Sample (Right) of Fracture Conductivity Sample

A gray resin is utilized for this step instead of a transparent resin, as laser profilometer scans performed on a transparent resin would be poor due to light scattering through the surface of the model. After support removal and post-processing completed, the sample was scanned in the laser profilometer to obtain the distribution of Z heights. We can then compare this distribution to that of the simulation parameters, as shown in the figure below:

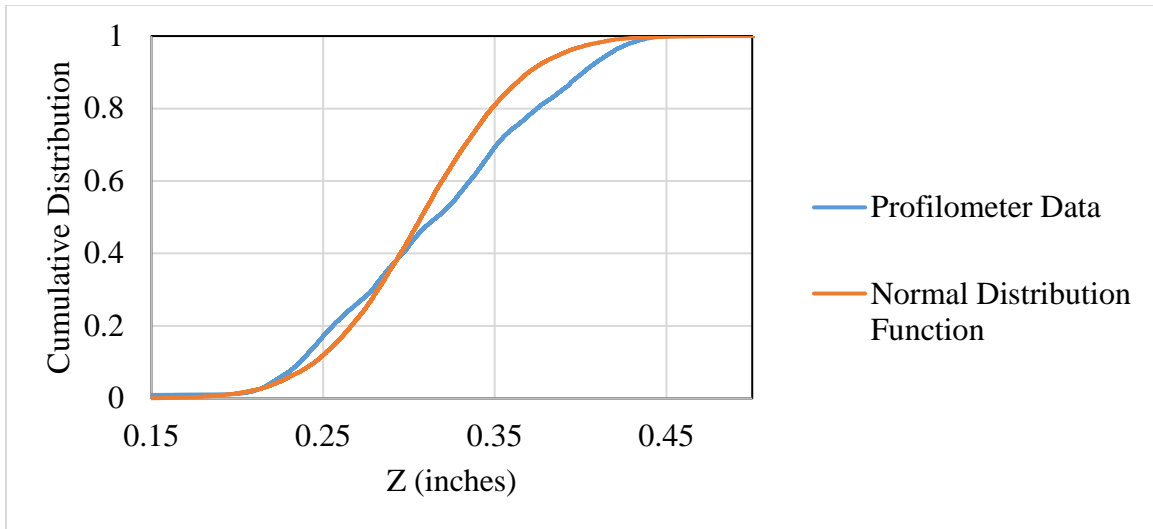


Figure 3.6 : Comparison of 3D Printed Profilometer Distribution and Modeled Distribution

Visual comparison of the sample to the digital model reveals the extremely fine details captured by the resin printer. Previous attempts at 3D printing these rough surfaces through traditional FDM approaches still possessed traces of visible layer lines. In contrast, the layer lines of the resin model produced from the SLA 3D printer are too small to see with the naked eye. Additionally, the profilometer data reveals that the distribution of surface points closely resembles that of the simulation inputs. After obtaining a satisfactory match and visually inspecting the quality of the model, the 3D printed samples could then be used to generate cement replicates for conductivity testing.

The cement samples were generated from the 3D printed models by pouring silicone casting material over the 3D printed conductivity samples. Once cured, the silicone mold is separated from the 3D printed conductivity sample, leaving behind a negative copy of the original surface imprinted in the silicone mold. Cement can be poured into this mold

and left to cure to create a replicate of the original sample. The quality of the cement replicas cast from the molds of the 3D printed samples is shown below in Figure 3.7:



Figure 3.7 : Cement replicas cast from mold of 3D printed conductivity samples

To ensure that the casting process did not lead to loss of resolution in the sample, a side-by-side profilometer scan (shown in Figure 3.8) was performed. Inspection of these two scans reveals identical surfaces between the two samples.

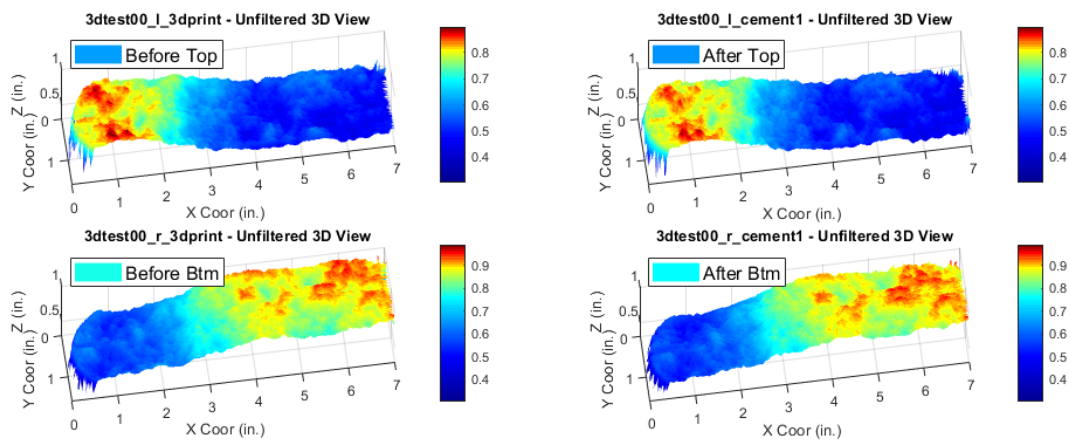


Figure 3.8 : Profilometer scans of 3D printed sample and cement replicas

The visual comparison of the profilometer scans paired with the comparison of the modeled distribution and the physical samples verify that the desired roughness was achieved in both the printed and cement samples. While the resolution of the profilometer is much less than that of the resolution of the printer (0.05 inches and 0.0029 inches, respectively), we can say with confidence that the similarities between the two sample surfaces at the profilometer resolution is satisfactory for use in future experiments for investigating surface roughness.

## 4. CONCLUSIONS & RECOMMENDATIONS

### 4.1 Conclusions

This thesis presents a developed workflow for integrating 3D printing technology into multiple facets of well stimulation research. While there are still multiple avenues to explore further at this time, the work presented in this study aims to lay the foundation for future research with the provided workflow and demonstrated application.

For this study, a workflow for simulating detailed fracture surfaces was presented before demonstrating the precision of the resulting 3D printed samples. Finally, the workflow developed for generating large, transparent fracture surfaces was tested. Based on these results, the following conclusions were made:

1. Resin 3D printing can serve as a valuable tool for producing numerous precise models in unconventional well stimulation research applications.
2. The workflows developed in this study can be utilized to produce consistent, accurate 3D prints of simulated surfaces.
3. 3D printed resin materials can maintain a level of clarity and rigidity that is more than sufficient for use in observation-based experiments, as demonstrated by the proppant transport apparatus.

## 4.2 Limitations, Recommendations, and Future Work

While this study was successfully able to develop a workflow for generating 3D printed files for specific use in well stimulation research, there are still limitations of the technology that must be acknowledged. For example, the degree to which the 3D printed fracture surfaces will erode over time from use in the proppant transport experiment has not yet been quantified. If the erosion is found to be severe after a considerably low number of tests, more expensive resins with tougher surfaces may need to be explored. Additionally, the process of refining the technique for recreating cement samples for use in fracture conductivity testing is actively ongoing. The following points are additional recommendations to consider for future work:

1. Generate multiple new large fracture apparatuses for testing in proppant transport experiments to analyze the degree to which surface roughness impacts the behavior of diverter and proppant transport.
2. Perform conductivity experiments on casts of the newly developed conductivity sample models. Furthermore, identify a suitable material for making consistent casts of the 3D printed conductivity samples for use in conductivity testing.
3. Investigate the effect of extreme features, such as large ridges, in both conductivity and proppant transport experiments using the artificial samples.

## REFERENCES

- Alotaibi, M., & Miskimins, J. L. (2020). Experimental Quantification of Slickwater Proppant Transport in Subsidiary Hydraulic Fractures. *International Petroleum Technology Conference*. Dhahran, Kingdom of Saudi Arabia.
- Alyafei, Nayef, Bautista, Jerahmeel, Mari, Sahar, . . . Seers, T. (2020). Multi-Dimensional Project Based Learning on Understanding Petrophysical Properties by Utilizing Image Processing and 3D Printing. *SPE Europec*.
- Anderson, T. (2016). Applications of Additive Manufacturing to Rock Analogue Fabrication. *SPE Annual Technical Conference and Exhibition*. Dubai, UAE.
- Bahri, A., & Miskimins, J. (2021). The Effects of Fluid Viscosity and Density on Proppant Transport in Complex Slot Systems. *SPE Virtual Hydraulic Fracturing Technology Conference*.
- Blat, H., Tracy, R., & Owens, B. (2006). *Petrology: Igneous, Sedimentary, and Metamorphic*. New York: W. H. Freeman.
- Camisa, J., Verma, V., Marler, D., & Madlinger, A. (2014). Additive Manufacturing and 3D Printing for Oil and Gas - Transformative Potential and Technology Constraints . *International Ocean and Polar Engineering Conference* (pp. 299-306). Busan, Korea: ISOPE.
- CBD-Tech. (2021). Chitubox Basic Ver. 1.7.0.
- Cooke Jr, C. (1973). Conductivity of Fracture Proppants in Multiple Layers. *Journal of Petroleum Technology*, 1101-1107.
- Dande, S., Stewart, R. R., & Dyaur, N. (2021). Effect of Fluids on the Elastic Properties of 3D-Printed Anisotropic Rock Models. In *Petrophysics Vol. 62* (pp. 537-552).

- Deutsch, C., & Journel, A. (2000). Geostatistical Software Library . Stanford University.
- Economides, M. J., Hill, A. D., Ehlig-Economides, C. . . . D. (2013). *Petroleum Production Systems, second edition*. NJ: Prentice Hall, Upper Saddle River.
- Elsarawy, A., & Nasr-El-Din, H. (2018). Propped Fracture Conductivity in Shale Reservoirs: A Review of its Importance and Roles in Fracturing Fluid Engineering. *SPE-192451-MS*.
- Guerra, J. (2019). *Fracture Conductivity Behavior in Shale Formations*. Thesis, Texas A&M University, Petroleum engineering, College station.
- Guerra, J., Zhu, D., & Hill, A. D. (2017). A Comparative Study of the Effects of Clay Content on the Fracture Conductivity of the Eagle Ford Shale and Marcellus Shale Formations. URTEC 2716913.
- Isleyen, E., & Duzgun, H. (2018). Evaluation of 3D Printing in Obtaining Replicates of Discontinuity Roughness. *ARMA 18-0015*.
- Jang, H., Kang, S., & Jang, B. (2014). Determination of Joint Roughness Coefficients Using Roughness parameters. *Rock Mechanics and Rock Engineering*, 2061-2073.
- Jiang, C., Zhao, G., Gao, M., & Zhao, Y. (2016). A Trial of 3D printing on Rock Dynamics. *Rock Dynamics: From Research to Engineering*.
- Jiang, Q., Feng, X., Song, L., Gong, Y., & Zheng, H. C. (2015). Modeling rock specimens through 3D printing: Tentative experiments and prospects. *Springer*, 101-111.
- Kelkar, M. (2002). Applied Geostatistics for Reservoir Characterization. Richardson, TX: Society of Petroleum Engineers.
- Kern, L. R., Perkins, T., & Wyant, R. E. (1959). The Mechanics of Sand Movement in Fracturing. *JPT*.



- Kulatilake, P., Balasingham, P., Park, J., & Morgan, R. (2006). Natural rock joint roughness quantification through fractal techniques. *Geotechnical and Geological Engineering*, 1181-1202.
- Luongo, A., V. Falster, Doest, M. B., Ribo, M. M., Eiriksson, E. R., Pedersen, D. B., & Frisvad, J. R. (2019). Microstructure Control in 3D Printing with Digital Light Processing. *Computer Graphics Forum*. Retrieved from Computer Graphics Forum: <https://doi.org/10.1111/cgf.13807>
- Marpaung, F. (2007). *Investigation of The Effect of Gel Residue on Hydraulic Fracture Conductivity Using Dynamic Fracture Conductivity Test*. Thesis, Texas A&M University, Petroleum Engineering, College Station, Texas.
- McDuff, D., Jackson, S., Shuchart, & C. (2010). *Understanding Wormholes in Carbonates: Unprecedented Experimental Scale and 3D Visualization*. *J Pet Technol*.
- Miskimins, J. (2019). *Hydraulic Fracturing Fundamentals and Advancements*. Society of Petroleum Engineers.
- Montgomery, C., & Smith, M. (2010). Hydraulic Fracturing: History of an Enduring. *Journal of Petroleum Technology*, 62(12), 26-32. doi:10.2118/1210-0026
- Mou, J. (2009). *MODELING ACID TRANSPORT AND NON-UNIFORM ETCHING*. College Station, TX: Texas A&M University.
- Mou, J., Zhu, D., & Hill, D. (2010). A New Acid Fracture Conductivity Model Based on the Spatial Distributions of Formation Properties. *SPE International Symposium and Exhibition on Formation Damage Control*. Lafayette ,LA: Society of Petroleum Engineers.

- Nieto, C. (2007). *3D Characterization of Acidized Fracture Surfaces*. Thesis, Texas A&M University, Petroleum Engineering, College Station.
- Obi, C. E. (2021). *Application of 3D Printing for Fracture Conductivity Testing*. College Station, TX: Texas A&M University.
- Olivera, S., Muralidhara, H., & Venkatesh, K. (2016). Evaluation of Surface Integrity and Strength Characteristics of Electroplated ABS Plastics using FDM Processes. *The 17 th Asian Pacific Corrosion Control Conference*. Mumbai, India.
- Palisch, T., Duenckel, R., Chapman, M., Woolfolk, S., & Vincent, M. (2010). How To Use and Misuse Proppant Crush Tests: Exposing the Top 10 Myths. *SPE Production & Operations*, 25(3): 345-354. , 345-354.
- Pournik, M., Zhu, D., & Hill, A. (2009). Acid-Fracture Conductivity Correlation Development Based on Acid-Fracture Characterization. *SPE European Formation Damage Conference*. Scheveningen, The Netherlands,: Society of Petroleum Engineers.
- Pyrzcz, M., H., J., Kuppenko, A., Liu, W., Gigliotti, A., Salomaki, T., & Santos, J. (2021). Geostats Py Package. Austin, TX.
- Raney, J. (2015). Printing mesoscale architectures. *MRS Bulletin*, 40(11), 943–950.
- Schwalbert, M. (August 2019). *Comprehensive Analysis of Acid Stimulation in Carbonates*. College Station, TX: Texas A&M University.
- Tatman, Bahri, Zhu, Hill, & Miskimins. (2022). Experimental Study of Proppant Transport Using 3D-printed Rough Fracture Surfaces. Houston, TX: SPE Annual Technical Conference & Exhibition.

- Tse, R., & Cruden, D. (1979). Estimating Joint Roughness Coefficients. *International Journal of Rock Mechanics and Mining Sciences & Geomechanics*, 303-307.
- Warpinski, N. (2009). Stress Amplification and Arch Dimensions in Proppant Beds Deposited by Waterfracs. *SPE 119350-PA* (pp. 461-471. ). SPE Production & Operations.
- Zhang, J. (2014). *Creation and Impairment of Hydraulic Fracture Conductivity in Shale Formations*. College Station, TX: Texas A&M University.
- Zhang, J. (2014). *Creation and Impairment of Hydraulic Fracture Conductivity in Shale Formations*. Thesis, Texas A&M University, Petroleum Engineering, College Station, Texas.

## APPENDIX A

### 3D Printing Nomenclature:

**Bottom Layer Count:** The number of layers designated to be overexposed to create a strong adhesion to the build plate, therefore laying a hard foundation for the model to be built up from. The value assigned here corresponds to the first 'X' layers of the print, and will ultimately be affected by other settings, like the bottom exposure time.

**Exposure Time:** Exposure time is the amount of time each layer will spend absorbing energy from the UV light array to cure and solidify. The longer a single layer is exposed, the more hardened it will become. Underexposure can lead to print failure, while overexposure is known to decrease overall print quality as it can suppress the finer details of the model.

**Bottom Exposure Time:** The bottom exposure time refers to the exposure time only applied to the bottom layers assigned in the bottom layer count. This distinction allows the user to set longer exposure time for just these layers, since they require more curing to properly adhere to the bed. Generally, it's recommended to set the bottom exposure 8 to 10 times longer than the normal exposure values.

**Lifting Distance:** The lift distance is the total length in millimeters that the build plate will travel, while the bottom lift distance is the same but applied only to the first layers (as assigned previously). While the default value of 10mm is typically fine, this value may need to be lowered slightly if bubbles begin to appear in clear or translucent resins, as this is likely caused by the model lifting too far out of the vat.

**Lift Speed:** The lift speeds are the rates at which the build plate is raised and lowered, in millimeters per minute. Lifting too fast can lead to supports breaking, as the current layer is mildly adhered to the FEP film after curing. Lifting too slowly will increase print time almost exponentially, since the extra duration adds up for every layer.

**Bottom Lift Speed:** This is the same as lift speed but only applied to the bottom layers. This value is typically much lower than the normal lift speed, as the bottom layers are cured for a longer period and are more adhered to the FEP film.

**Retract Speed:** In Chitubox, this parameter describes the downwards speed of the build plate, which is usually set much faster than the lift speed. The default is set to 150 mm/min.